

Journal of Geophysical Research: Oceans

RESEARCH ARTICLE

10.1002/2015JC011089

Special Section:

Physical Processes Responsible for Material Transport in the Gulf of Mexico for Oil Spill Applications

Key Points:

- A large eddy simulation is used to study the effects of multiscale turbulence on ocean tracers
- Passive tracer mixing depends on air-sea tracer flux rate, tracer release depth, and flow regime
- Suppressed turbulent mixing by submesoscale eddies leads to reduced entrainment of tracers

Correspondence to:

K. M. Smith,
katherine.smith-1@colorado.edu

Citation:

Smith, K. M., P. E. Hamlington, and B. Fox-Kemper (2016), Effects of submesoscale turbulence on ocean tracers, *J. Geophys. Res. Oceans*, 120, doi:10.1002/2015JC011089.

Received 29 JUN 2015

Accepted 21 DEC 2015

Accepted article online 26 DEC 2015

Effects of submesoscale turbulence on ocean tracers

Katherine M. Smith¹, Peter E. Hamlington¹, and Baylor Fox-Kemper²

¹Department of Mechanical Engineering, University of Colorado at Boulder, Boulder, Colorado, USA, ²Department of Earth, Environmental, and Planetary Sciences, Brown University, Providence, Rhode Island, USA

Abstract Ocean tracers such as carbon dioxide, nutrients, plankton, and oil advect, diffuse, and react primarily in the oceanic mixed layer where air-sea gas exchange occurs and light is plentiful for photosynthesis. There can be substantial heterogeneity in the spatial distributions of these tracers due to turbulent stirring, particularly in the submesoscale range where partly geostrophic fronts and eddies and small-scale three-dimensional turbulence are simultaneously active. In this study, a large eddy simulation spanning horizontal scales from 20 km down to 5 m is used to examine the effects of multiscale turbulent mixing on non-reactive passive ocean tracers from interior and sea-surface sources. The simulation includes the effects of both wave-driven Langmuir turbulence and submesoscale eddies, and tracers with different initial and boundary conditions are examined in order to understand the respective impacts of small-scale and submesoscale motions on tracer transport. Tracer properties are characterized using spatial fields and statistics, multiscale fluxes, and spectra, and the results detail how tracer mixing depends on air-sea tracer flux rate, tracer release depth, and flow regime. Although vertical fluxes of buoyancy by submesoscale eddies compete with mixing by Langmuir turbulence, vertical fluxes of tracers are often dominated by Langmuir turbulence, particularly for tracers that are released near the mixed-layer base or that dissolve rapidly through the surface, even in regions with pronounced submesoscale activity. Early in the evolution of some tracers, negative eddy diffusivities occur co-located with regions of negative potential vorticity, suggesting that symmetric instabilities or other submesoscale phenomenon may act to oppose turbulent mixing.

1. Introduction

The ocean is estimated to store over 20% of all anthropogenic CO₂ and over 90% of anthropogenic heat [Sabine, 2004; Khatiwala *et al.*, 2013] and is the largest reservoir of carbon in the Earth system that is active on short time scales. In order to more accurately represent the ocean carbon cycle in global climate models, however, an improved understanding of the evolution and properties of biogeochemical tracers such as CO₂, phytoplankton, and zooplankton is required [Archer, 1995]. Each of these tracers can be conceptualized as an Eulerian concentration field (as opposed to discrete Lagrangian particles) that is advected by the fluid flow. The evolution of such tracers occurs primarily in the oceanic mixed layer where light is plentiful, air-sea exchanges of energy, momentum, gases, and freshwater occur [e.g., Bates *et al.*, 2012], and both three-dimensional small-scale turbulent mixing and quasi two-dimensional submesoscale turbulent transport are active in transporting tracers vertically. The evolution and properties of mixed-layer tracers are thus closely coupled to the dynamics of upper ocean turbulence.

Even when ocean tracers are passive (i.e., their concentration does not affect density or otherwise change the flow), their coupling to multiscale mixed-layer turbulence is not trivial. As an example of this complex coupling, the supply of CO₂ across the air-sea interface depends on the rate at which vertical mixing transports CO₂ downward, thereby maintaining (or, conversely, failing to maintain) a favorable air-sea gradient for diffusion of CO₂ across the surface [Watson and Orr, 2003]. Reactions between tracer species and heterogeneities in reaction rates result in even more complex systems. For example, phytoplankton are most productive near the surface where light is plentiful for photosynthesis, but in order to grow they require that nutrients be brought upward from stores at depth. The dispersion of buoyant oil, which often collects at the surface after accidental spills, is yet another example of turbulent tracer transport across many scales of upper ocean motion.

It is well known from prior observational [Gower *et al.*, 1980; Strass, 1992; Yoder *et al.*, 1992; Denman and Abbott, 1994; McGillicuddy *et al.*, 2001; Strutton *et al.*, 2012; Clayton, 2013] and numerical [Powell and Okubo, 1994;

Abraham, 1998; Bees, 1998; Mahadevan and Archer, 2000; Martin et al., 2002; Mahadevan and Campbell, 2002; Mahadevan, 2005; Tzella and Haynes, 2007; Levy and Klein, 2015] studies that the coupling between biogeochemical tracers and fluid processes results in heterogeneous distributions of tracers at the ocean surface. The origins and characteristics of this heterogeneity are understood to have potential biological and physical origins, particularly at small (i.e., subkilometer) scales. However, these prior studies have also revealed a major unresolved difficulty in fully describing the origins of tracer heterogeneity: namely, understanding and explaining the impacts of multiscale turbulent fluid processes on tracer evolution, and the “solubility” and “biological” carbon pumps in particular. Addressing this difficulty is the primary motivation for the present study.

The range of fluid scales relevant to ocean tracer evolution is truly enormous. Ocean biogeochemistry is affected by fluid processes that span basin-scale ($\sim 10,000$ km) budgets to millimeter-scale flows where kinetic energy and tracer variance are dissipated [Smyth, 1999; Lewis, 2005]. Many important fluid processes take place between these scales, and processes at widely disparate scales may also interact [Hamlington et al., 2014; Haney et al., 2015; McWilliams et al., 2015]. At relatively large scales, recent studies have shown that physical transport by mesoscale (~ 100 km) and submesoscale (~ 1 – 10 km) circulations can give rise to substantial tracer heterogeneity [Strass, 1992; Mahadevan and Archer, 2000; Levy et al., 2001; Mahadevan and Campbell, 2002, 2003; Mahadevan et al., 2012b]. In particular, prior studies [McGillicuddy et al., 1998; Follows and Williams, 2003; Mahadevan et al., 2012a; Omand et al., 2015] have revealed that upwelling associated with mesoscale and submesoscale fronts plays a key role in nutrient transport, phytoplankton production, and bloom timing and budgets. These upwelling motions produce $\mathcal{O}(1\text{ km})$ variations in tracer distributions at the surface, which are also affected by biological and chemical processes.

By contrast to prior studies focused on the effects of larger-scale ocean processes on tracer dynamics, the present study is specifically focused on the effects of submesoscale turbulent processes from meter to kilometer scales. The scale range emphasized here includes mixed-layer restratification involving coherent vertical motions of water masses by $\mathcal{O}(1$ – 10 km) submesoscale eddies and wind and wave-influenced fronts and vertical mixing by $\mathcal{O}(1\text{ m}$ – $1\text{ km})$ Langmuir turbulence. These processes occur at subgrid scales in essentially all global climate models, and thus an improved understanding of their effects on tracer dynamics will assist in the development of improved physically accurate subgrid-scale tracer parameterizations.

Although submesoscale eddies and Langmuir turbulence commonly involve similar horizontal velocities of $\mathcal{O}(0.1\text{ m/s})$, their typical vertical velocity scales, and hence their ability to transport tracers, differ substantially. The ratio of horizontal to vertical length scales is $\mathcal{O}(1)$ for Langmuir cells, so the largest horizontal separation distance between these cells tends to vary with mixed-layer depth [Smith, 1992]. The corresponding ratio of horizontal to vertical velocity scales is also $\mathcal{O}(1)$ for Langmuir cells. Submesoscale eddies, by contrast, tend to occur on horizontal scales near the mixed-layer deformation radius [Boccaletti et al., 2007; Thomas et al., 2008], so they are much wider than the mixed-layer depth, with a horizontal to vertical length scale ratio of $\mathcal{O}(N/f)$, where N and f are the buoyancy frequency and Coriolis parameter magnitude, respectively. Such eddies are roughly 10–100 times wider than the mixed layer is deep under typical upper ocean stratification, mixing, and frontal strength conditions [Tandon and Garrett, 1994; Haine and Marshall, 1998; Haney et al., 2012]. Furthermore, geostrophic flows avoid horizontal convergence and are therefore associated with small vertical velocities, so weaker submesoscale fronts and eddies (i.e., those with small Rossby number) have horizontal to vertical velocity-scale ratios that are even greater than N/f [McWilliams, 1985]. During frontogenesis, the vertical velocity can be significantly larger at the nose of the front due to the frontal overturning circulation, and this velocity is further enhanced during the creation of fronts aligned with the Stokes drift (N. Suzuki and B. Fox-Kemper, Understanding Stokes Forces in the Wave-Averaged Equations, submitted 2015).

In the present study, a large eddy simulation (LES) is performed in order to examine the effects of submesoscale ocean processes on the evolution of tracers in the oceanic mixed layer at horizontal scales from 20 km down to 5 m, with a specific focus on the respective roles played by submesoscale eddies, as well as their associated fronts, and Langmuir turbulence. Hamlington et al. [2014] examined the same range of scales with a focus on the interactions between submesoscale processes and small-scale Langmuir turbulence, finding that the effects of Langmuir turbulence are weakened in the presence of submesoscale eddies. Contrasts will be made here between tracer behavior in regions where both submesoscale eddies and Langmuir turbulence are active, and in regions where only Langmuir turbulence is active. Submesoscale motions are

coherent on larger scales than Langmuir turbulence, so spectral analysis of fluxes and tracer variance will also be used to understand tracer evolution and properties.

Although real-world upper ocean tracers have substantial dynamical complexity, the present study employs a foundational approach whereby nonreactive passive tracers are modeled in the presence of realistic upper ocean turbulence for a wide range of tracer conditions. This approach is intended to reveal fundamental effects of upper ocean fluid transport processes on tracer evolution and distributions prior to increasing the complexity of the modeled tracers (e.g., by employing reactive chemistry or coupled nutrient, phytoplankton, and zooplankton dynamics). Tracers examined in the present study include nonconserved tracers that flux across the air-sea interface and conserved tracers released at different initial locations in the mixed layer. These tracers have been specifically chosen to represent biogeochemical tracers such as CO₂, phytoplankton, and oil, whose dynamics can be idealized as vertical transport problems. Such transport has a substantial impact on tracer heterogeneity, but there are a number of outstanding questions that must still be answered, including:

1. How is near-surface CO₂ flushed downward after diffusing across the air-sea interface?
2. How do phytoplankton arrive in the euphotic zone?
3. How are nutrients delivered to the euphotic zone from greater depths?

The present study will address key aspects of each of these questions by modeling the transport of idealized tracers in the presence of realistic submesoscale ocean flows that are spatially heterogeneous in horizontal directions and that also vary with scale. A range of different tracer flux rates and initial source locations will be examined in order to develop a parametric understanding of tracer evolution and properties, which will be of substantial benefit when using the present results to inform the development of new subgrid models for tracer transport.

It should be noted that, due to the multiscale nature of biogeochemical tracer dynamics in the oceanic mixed layer, previous studies have often focused on increasing the complexity of biogeochemical modeling while employing relatively simple background flows [e.g., Abraham, 1998; Denman, 2003; Tzella and Haynes, 2007; Benzi and Nelson, 2009; Pigolotti *et al.*, 2012]. Therefore, the present study of idealized tracers in complex flows has complementary aims to those studying more complex tracer dynamics in simple flows. This study will, in turn, provide baseline knowledge concerning the impacts of multiscale oceanic fluid dynamics on tracer heterogeneity.

In the following, details of the numerical simulation are outlined first, followed by a presentation of results from the simulation. These results are then discussed in the context of modeling tracer properties using eddy diffusivity approaches and understanding the patchiness of biological tracers such as phytoplankton. Finally, conclusions are provided at the end of the paper.

2. Numerical Simulation

The numerical simulation performed in the present study is an extension of the submesoscale frontal spin-down simulations described in Hamlington *et al.* [2014]. The governing equations solved are the wave-averaged Boussinesq equations [Craik and Leibovich, 1976; Gjaja and Holm, 1996; Holm, 1996; McWilliams *et al.*, 2004; (N. Suzuki, B. Fox-Kemper, P. E. Hamlington, and L. P. Van Roekel, Surface Waves Affect Frontogenesis, submitted 2015)] given by

$$\frac{D\mathbf{u}}{Dt} = -\nabla p - \mathbf{f} \times \mathbf{u}_L - u_{Lj} \nabla u_{sj} + b\hat{\mathbf{z}} + \mathbf{SGS}_u, \quad (1)$$

$$\frac{Db}{Dt} = \mathbf{SGS}_b, \quad (2)$$

$$\frac{Dc_i}{Dt} = \mathbf{SGS}_{ci}, \quad (3)$$

$$\nabla \cdot \mathbf{u} = 0, \quad (4)$$

where $D/Dt \equiv \partial/\partial t + (\mathbf{u}_L \cdot \nabla)$ is the Lagrangian material derivative, \mathbf{u} is the Eulerian velocity averaged over surface gravity waves, \mathbf{f} is the Coriolis parameter, p is the pressure normalized by a reference density ρ_0 , b is

Table 1. Summary of Physical and Computational Parameters Used in the Numerical Simulation^a

Physical size, $L_x \times L_y \times L_z$	20 km \times 20 km \times -160 m
Grid size, $N_x \times N_y \times N_z$	4096 \times 4096 \times 128
Grid resolution, $\Delta_x \times \Delta_y \times \Delta_z$	4.9 m \times 4.9 m \times 1.25 m
Reference density, ρ_0	1000 kg/m ³
Coriolis parameter, f	0.729 \times 10 ⁻⁴ s ⁻¹ \hat{z}
Initial mixed-layer depth, $H_{ML,0}$	-50 m
Wind speed at 10 m, U_{10}	5 m/s
Stokes drift velocity, $u_s(z = 0 \text{ m})$	0.063 m/s
Turbulent Langmuir number, La_t	0.29
Stokes drift direction, ϑ_s	30°
Wind friction velocity, u_τ	5.46 \times 10 ⁻³ m/s
Wind shear, τ	0.025 N/m ²
Wind direction, ϑ_w	30°

^aThe turbulent Langmuir number is defined as $La_t = \sqrt{u_\tau/u_s(0)}$.

the buoyancy, $\mathbf{u}_L \equiv \mathbf{u} + \mathbf{u}_s$ is the Lagrangian velocity, and \mathbf{u}_s is the Stokes drift velocity created by surface gravity waves. Buoyancy is given as $b = -g\rho/\rho_0$, where g is gravitational acceleration, ρ is density, and b has dimensions of acceleration. Buoyancy frequency is related to buoyancy by $N^2 = \partial b / \partial z$. The third term on the right-hand side of equation (1) is the Stokes shear force, which has been written using index notation for clarity (N. Suzuki and B. Fox-Kemper, Understanding Stokes Forces in the Wave-Averaged Equations, submitted 2015). In equation (3), c_i denotes the Eulerian concentration field for the i th tracer. The tracers considered in the present study are all nonreactive and thus there are no source terms on the right-hand side of equation (3). The tracers are also passive and thus do not impact the dynamics of the velocity \mathbf{u} or the buoyancy b . Each of the SGS_i terms in equations (1–3) are vector fluxes representing the subgrid-scale (SGS) model used in the LES. Parameter values used in the simulation are summarized in Table 1.

The Stokes drift velocity \mathbf{u}_s in equations (1–3) is represented in the simulation as

$$\mathbf{u}_s(z) = u_s(z)[\cos(\vartheta_s)\hat{\mathbf{x}} + \sin(\vartheta_s)\hat{\mathbf{y}}], \quad (5)$$

where $u_s(z)$ is the Stokes drift magnitude vertical profile, which decays faster than exponentially from the surface, and ϑ_s is the angle of the Stokes drift velocity in the horizontal (i.e., x - y) plane. The mathematical formulation for $u_s(z)$ is given by numerical integration of the wave spectrum in *Donelan et al.* [1985, equation (5.1)] and *Webb and Fox-Kemper* [2011, equation (33)], and is shown in Figure 1 as a function of depth.

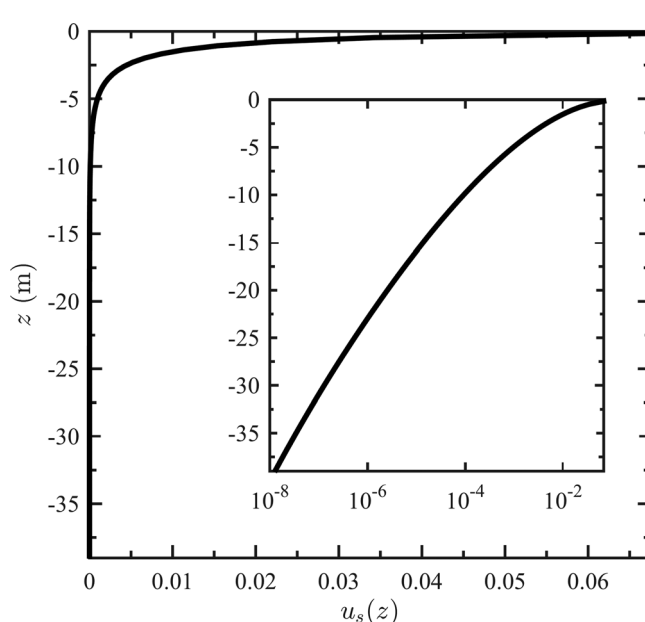


Figure 1. Stokes drift velocity $u_s(z)$ used in equation (5) as a function of depth z . The main plot shows $u_s(z)$ on linear axes and the inset shows $u_s(z)$ on semilog axes.

Note that the Stokes drift velocity \mathbf{u}_s is the same at all horizontal locations and depends only on z . Wave spreading effects on Stokes drift are neglected [Webb and Fox-Kemper, 2015], as are breaking wave effects. Prior studies [McWilliams et al., 1997; Van Roekel et al., 2012; Hamlington et al., 2014] have shown that this parameterization for the Stokes drift velocity leads to the creation of small-scale, counterrotating Langmuir cells throughout the domain, with the strongest cells occurring close to the surface (i.e., within the upper 25 m of the ocean), and substantial impacts on submesoscale fronts and instabilities [McWilliams and Fox-Kemper, 2013; Haney et al., 2015; (N. Suzuki and B. Fox-Kemper, Understanding Stokes Forces in the Wave-Averaged Equations, submitted to J. Geophys. Res., 2015)].

The numerical model used to solve the governing equations is the National Center for Atmospheric Research (NCAR) LES model [Moeng, 1984] which is described in McWilliams *et al.* [1997] and Sullivan *et al.* [2007]. Horizontal spatial derivatives are calculated spectrally, while second-order finite differences are used for vertical velocity derivatives and third-order finite differences are used for vertical tracer derivatives. A third-order Runge-Kutta time stepping scheme is used with a constant Courant number. Essentially the same model has been used in several prior studies [e.g., McWilliams *et al.*, 1997; Sullivan *et al.*, 2007; Van Rœkel *et al.*, 2012; Hamlington *et al.*, 2014].

The LES is performed using a subgrid-scale model for the SGS terms in equations (1–3) that provides a spatially variable viscosity, buoyancy diffusivity, and tracer diffusivity according to the scheme proposed by Sullivan *et al.* [1994]. As a result, there is no one tracer diffusivity or viscosity applied throughout the domain. A ratio between the tracer transport by the subgrid scheme and by the resolved flow can be formed and interpreted as a Péclet number (the Schmidt number, relating subgrid viscosity to diffusivity, is fixed at 1/3 by the subgrid-scale model [Sullivan *et al.*, 1994] and applies to both buoyancy and passive tracers). The horizontal Péclet number is 3.2 on 100 m scales and 1262 on 10 km scales. The vertical Péclet number is 1.3 using basin-averaged root-mean-square velocity and 50 m mixed-layer depth. In the real ocean, the equivalent quantities are 10^5 , 10^7 , and 10^4 , respectively. It is therefore likely that the subgrid scheme does affect the tracer transport significantly on small scales, particularly in the vertical direction, so the transport by Langmuir turbulence is likely to be quantitatively different when compared to a simulation with higher resolution. It is important to recognize, however, that variability in the subgrid diffusivity is intended to resemble a spectral variance cascade, so it may behave like a higher Péclet number flow, or in any case quite differently from a flow with constant diffusivity. The Péclet number of submesoscale features is very large, and so the interaction between submesoscale eddies and Langmuir turbulence crosses a range of scales where diffusivity is weak, as in the real ocean. The computational expense of the present simulation precludes a comparison to higher-resolution simulations, but in a smaller domain the effects of the subgrid scheme and finite Péclet number may be explored in the future.

The physical setup for the current study is the spin-down of two submesoscale buoyancy fronts; the same configuration has been examined previously in Hamlington *et al.* [2014]. In the Hamlington *et al.* [2014] study, a warm 10 km wide filament of water was initialized within a domain of cooler water. Oblique wind and wave forcing was applied at a horizontal angle of 30°, leading to destabilization of the more buoyant filament along an unstable front where the Ekman buoyancy flux from the downfront wind component carries more dense water over less dense water, resulting in the formation of $\mathcal{O}(5 \text{ km})$ submesoscale eddies. A stable front on the other side of the buoyant filament is restratified by an upfront wind and Ekman buoyancy flux of less dense water carried over more dense water [Thomas and Lee, 2005]. A mixed-layer region was initialized near the surface of the domain with an initial uniform depth of $H_{ML,0} = -50 \text{ m}$. The mixed layer becomes both significantly deeper and shallower at different spatial locations as the system evolves. Substantial additional detail on the spin-down configuration and the subsequent evolution of the system is provided in Hamlington *et al.* [2014].

The present study builds upon the simulations described in Hamlington *et al.* [2014] by introducing tracers to the simulation and restarting the computations at roughly day 12, corresponding to the final fully developed state in the Hamlington *et al.* [2014] study. Figure 2 shows the buoyancy field at day 12 when the tracers are first introduced. At this time, a number of large submesoscale eddies have formed, but the eddies along the unstable front have not yet begun to interact with the stable front. The same wave and wind forcing is maintained after restarting the simulation, corresponding to a surface wind stress with wind speed of 5 m/s and an angle of 30° with respect to the x axis (which is aligned with the initial along-front orientation of the buoyancy filament). Additionally, the original uniform mixed-layer depth of -50 m has been modified throughout the domain by the deepening effects of Langmuir turbulence and the shallowing effects of restratifying submesoscale eddies. At the time of tracer introduction, the mixed-layer depth based on the buoyancy threshold $\Delta b > (\Delta b)_c$, where $\Delta b \equiv [b(x,y,0) - b(x,y,z)]$ and $(\Delta b)_c = -0.53 \text{ m s}^{-2}$, ranges from roughly -30 to -55 m . The mixed-layer depth based on the critical Richardson number $Ri_c = 0.25$ ranges from -20 to -40 m , and the depth based on the Ertel potential vorticity threshold $q(x,y,z) > q_c$ where $q_c = 8 \times 10^{-11} \text{ s}^{-3}$, ranges from -30 to -60 m . These different depths indicate a variety of mixing processes, including convective, Langmuir, and symmetric instabilities [Taylor and Ferrari, 2010a; Hamlington *et al.*, 2014; Haney *et al.*, 2015].

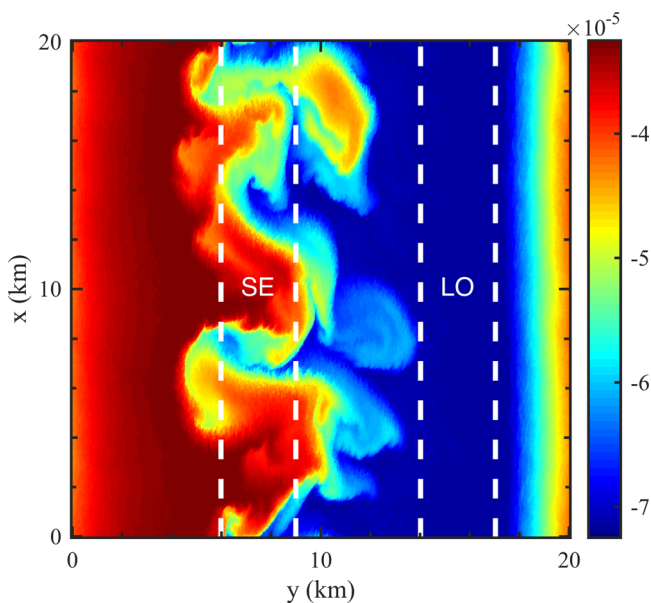


Figure 2. Initial x-y surface buoyancy field when tracers are introduced to the simulation, corresponding to approximately day 12 of the Hamlington *et al.* [2014] study. Vertical white dashed lines denote the Langmuir only (LO) and submesoscale eddy (SE) regions over which statistics are calculated.

the spin-down problem, thereby allowing the simultaneous effects of submesoscale eddies and Langmuir turbulence to be studied prior to interaction of the stable and unstable fronts, which begins to occur near day 14. Analysis of tracer fields in this study has been primarily performed 8 h after the tracers are introduced to the simulation. This particular time is chosen for the analysis in order to allow sufficient time for the tracer fields to develop so that robust insights into tracer evolution can be obtained, while also avoiding later times when the unstable and stable fronts begin to interact. Although the spin-down configuration examined here is an inherently nonstationary problem, all qualitative trends and conclusions obtained from results at 8 h have been checked for robustness by comparing with results at other times. Any cases where trends and conclusions change substantially as functions of time are noted in the text.

Twelve different tracer fields are introduced to the simulation at day 12: (i) five passive air-sea boundary flux tracers (referred to as c_{Hi} , where $i=1, 2, \dots, 5$) and (ii) seven passive, initial finite source tracers (referred to as c_{lj} , where $j=1, 2, \dots, 7$). The air-sea boundary flux tracers, summarized in Table 2, each have specified flux rates across the upper boundary given by Henry's law for diffusive flux of a gas across the air-sea interface [Wanninkhof, 1992; Liss and Johnson, 2014], namely

$$F_i = k_i(c_{air} - c_{Hi,0}), \quad (6)$$

where F_i is the downward flux rate across the boundary for the i th air-sea tracer (i.e., c_{Hi}), k_i is the tracer flux rate, or piston velocity, for each tracer, c_{air} is the concentration in air, or the partial pressure of the gas to be dissolved just above the boundary scaled by the Henry's law constant, and $c_{Hi,0}$ is the gas concentration c_{Hi} just below the boundary (initialized to 0 at the start of the simulation). The value of c_{air} is fixed at 1 in this study.

Table 2. Summary of Tracers Diffused Across the Air-Sea Interface According to Henry's Law in Equation (6), Showing the Tracer Flux Rate, k_i , and Corresponding Characteristic Transfer Time Scale, τ_i^a

Tracer c_{Hi}	k_i ($m s^{-1}$)	τ_i (s)	τ_S/τ_i	τ_L/τ_i
c_{H1}	2×10^{-2}	2.5×10^3	8×10^3	4
c_{H2}	2×10^{-3}	2.5×10^4	8×10^2	4×10^{-1}
c_{H3}	2×10^{-4}	2.5×10^5	8×10^1	4×10^{-2}
c_{H4}	2×10^{-5}	2.5×10^6	8	4×10^{-3}
c_{H5}	2×10^{-6}	2.5×10^7	8×10^{-1}	4×10^{-4}

^aRatios of characteristic large-scale τ_S and small-scale τ_L fluid time scales relative to $\tau_i = h/k_i$ are also shown, where $\tau_S = h/w_s \approx 2 \times 10^7$ s [Fox-Kemper *et al.*, 2008] and $\tau_L = h/\sqrt{\langle w^2 \rangle} \approx 10^4$ s.

The physical domain size of the simulation is $20 \text{ km} \times 20 \text{ km} \times -160 \text{ m}$, with a computational grid of size $4096 \times 4096 \times 128$, giving a horizontal resolution of $\sim 5 \text{ m}$ and a vertical resolution of $\sim 1 \text{ m}$ (a summary of these and other simulation parameters is provided in Table 1). For the Eulerian velocity field \mathbf{u} , periodic boundary conditions are used in horizontal (x - y) directions, with no vertical velocity and a wind stress condition at the top boundary, and a stress-free condition at the bottom boundary. In the present study, the simulation was run for approximately 60 additional hours past the initial day 12 starting point; beyond 60 h, submesoscale eddies along the unstable front have grown large enough to strongly affect the stable front. As shown in Hamlington *et al.* [2014], substantial submesoscale structure has developed by day 12 of

Each of the five air-sea flux tracers has a different constant value of k_i , as shown in Table 2. The range of tracer flux rates k_i for c_{H1} – c_{H5} in Table 2 has been chosen to span a range of time scales that match the characteristic time scales of both submesoscale eddies, where $\tau_s \approx 10^7$ s, and Langmuir turbulence, where $\tau_L \approx 10^4$ s. They can also be interpreted as representing a range of Schmidt (Sc) numbers for different gases, using the formula of Wanninkhof [1992] and the 5 m/s wind speed corresponding to the modeled wind stress, namely

$$k_i = 0.31 u^2 \sqrt{\frac{660}{Sc}}. \quad (7)$$

This relation already includes the effects of ocean turbulence to some degree as it is based on observations (see the discussion in Calmet and Magnaudet [1998]), while here turbulence plays an active role in setting the flux rate. These values should only be considered as a guide to order of magnitude. With this caveat, the Schmidt number for the fastest air-sea velocity ranges from 10^{-3} for c_{H1} to 10^5 for c_{H5} . Thus, for typical gases (e.g., CO₂, oxygen, and chlorofluorocarbons) and typical surface seawater temperature and salinity, the c_{H3} and c_{H4} tracers span the realistic range (where $Sc = 660$ for CO₂ in seawater at 20°C [Wanninkhof, 1992]). A wider range of values is used, so that the effects of transfer fast enough to rival Langmuir turbulence and slow enough to rival submesoscale processes can be examined. With these values for k_i , the ratio τ_s/τ_i extends from 8×10^3 to 8×10^{-1} when going from c_{H1} to c_{H5} , while τ_L/τ_i extends from 4 to 4×10^{-4} from c_{H1} to c_{H5} . Whenever these ratios are $\mathcal{O}(1)$, we may expect strong interactions between fluid dynamics and tracer uptake, so the present range of air-sea flux velocities crosses this threshold for both Langmuir and submesoscale turbulence. The choice of values for k_i in Table 2, combined with the scale separation between submesoscale and Langmuir processes enabled by the wide range of scales in the simulation, allows an examination of the separate effects of submesoscale eddies and small-scale Langmuir turbulence on tracer distributions and evolution. All of the tracer fluxes in the simulation are observed to be exclusively from the air to the ocean, thus assuming an infinite reservoir of tracer and a rapid refreshing of the surface air above the ocean. Each of the tracers have periodic boundary conditions in horizontal directions, with no vertical fluxes at the bottom boundary and top boundary fluxes given by equation (6).

In a well-mixed layer of approximately constant depth h , the concentration of a tracer c_{Hi} subject to the flux law specified in equation (6) should increase as

$$c_{Hi} = c_{air} \left(1 - e^{-tk_i/h} \right) = c_{air} \left(1 - e^{-t/\tau_i} \right). \quad (8)$$

Thus, in Table 2, the time scale $\tau_i = h/k_i$ is used to categorize the rate of air-sea flux, where h is estimated as the initial mixed-layer depth of –50 m. This time scale is compared to $\tau_L = O(h/\sqrt{\langle w^2 \rangle})$ based on Langmuir vertical velocities from the simulation and $\tau_s \approx h/w_s$, where w_s is estimated as the eddy-induced vertical velocity resulting from the restratification stream function of Fox-Kemper et al. [2008]. If there is no turbulent transport or mixing, then only the surface grid cell would absorb tracer and it would saturate $h/\Delta z$ times faster, followed by spreading across the mixed layer on much slower diffusive time scales. For mixed layers that have not yet become fully saturated with tracer, turbulent diffusion provides much more rapid transport away from the surface, thereby maintaining a greater air-sea flux rate since surface waters are continually refreshed. It should be noted, however, that after the entire mixed layer becomes fully saturated, the air-sea flux rate will decrease regardless of the effects of turbulent diffusion, since only through the slow process of entrainment of water from below the mixed layer can any tracer-free water be brought near the surface.

The initial finite source tracers, denoted c_{ij} , are conserved after their introduction to the domain at day 12, unlike the air-sea flux tracers. These finite source tracers are distinguished by their different initial source locations, where the initial condition is given as

$$c_{ij}(\mathbf{x}, t_0) = \begin{cases} 1 & \text{if } z = z_j \\ 0 & \text{otherwise} \end{cases}, \quad (9)$$

where t_0 denotes the initial time and z_j is the depth at which the tracer is introduced. The tracer concentration is initially uniform for all x and y at the given depth z_j , and the tracers are initialized over two grid cells in the vertical direction, giving an initial tracer field of depth 2.5 m. The different values of z_j for the tracers in the present simulation are given in Table 3, where c_{i1} is a tracer released at the surface, c_{i7} is released at $z = -60$ m, which is below the initial pycnocline of $H_{ML,0} = -50$ m, and the other five initial source tracers

Table 3. Summary of Tracers Released at Different Locations in the Oceanic Mixed Layer^a

Tracer c_j	Physical Location	z_j (m)	$z_j/H_{ML,0}$
c_{j1}	Surface	0	0
c_{j2}	Shallow mixed layer	-10	0.2
c_{j3}	Middle mixed layer 1	-20	0.4
c_{j4}	Middle mixed layer 2	-30	0.6
c_{j5}	Deep mixed layer	-40	0.8
c_{j6}	At initial pycnocline	-50	1
c_{j7}	Below initial pycnocline	-60	1.2

^aThe initial tracer locations z_j are normalized in the last column by the initial mixed-layer depth in the simulation, $H_{ML,0} = -50$ m.

are incrementally distributed at different depths within the mixed layer. Two of the finite initial concentration tracers (c_{j1} and c_{j7} , respectively) have been chosen to represent the initial source locations of tracers that typically originate at the surface, such as phytoplankton, and tracers typically stored at depth, such as nutrients. Tracers c_{j5} and c_{j6} are initialized at depths near which the pycnocline undergoes substantial variations due to the interplay between submesoscale eddies and Langmuir turbulence. At these depths, the influence of the near-surface convective boundary layer and a deeper layer unstable to symmetric instabilities, which are associated with submesoscale eddies, compete and give rise to widely different tracer distributions. Once again, each of the tracers have periodic boundary conditions in horizontal directions, but for the initial source tracers there are zero vertical flux conditions at both the top and bottom boundaries.

It should be noted that although the tracers included in the simulation are idealized, they are intended to provide insights into tracers relevant to the biogeochemistry of the upper ocean. The air-sea flux tracers provide insights into transport of chemical species and gases transferred at the air-sea interface. Similarly, the initial source tracers provide insights into biologically relevant tracers that reside near the surface, such as phytoplankton or oil (e.g., c_{j1} and c_{j2}), and at depth, such as nutrients (e.g., c_{j6} and c_{j7}). The use of idealized tracers in the current study is consistent with the present focus on understanding the fundamental interactions between passive tracers and realistic submesoscale ocean turbulence. The tracers themselves are idealized in order to perform a parametric study of the effects of different initial source locations and surface flux rates on tracer properties. In the future, the present results will inform understanding of distributions and the evolution of more realistic tracers in the upper ocean.

3. Properties of Mixed-Layer Tracers

Four primary metrics are used in the present analysis to examine the properties and evolution of tracers in the upper ocean: (i) three-dimensional (3-D) concentration fields, which provide a qualitative understanding of tracer distributions, (ii) vertical profiles of x - y -averaged tracer concentrations, variances, and vertical fluxes, (iii) one-dimensional (1-D) spectra calculated in the along-front direction (i.e., the x direction, see Figure 2), and (iv) multiscale vertical fluxes of both active (i.e., buoyancy) and passive tracers. In the following, these metrics are calculated for the air-sea flux tracers c_{H1} – c_{H5} (summarized in Table 2) and for the initial source tracers c_{j1} – c_{j7} (Table 3). Additional tracer properties related to modeling of tracer transport and phytoplankton production are examined in later sections.

The analysis herein is performed separately for different subsets of the domain, as shown in Figure 2. These subsets include the small-scale turbulence-dominated region between $y \approx 14$ –17 km in Figure 2 and the combined small-scale turbulence and large-scale eddy region between $y \approx 6$ –9 km. The bounds of these regions are adjusted as the simulation progresses and the unstable front shifts to smaller y as a result of Ekman transport. These two regions are referred to in the following as the Langmuir only (LO) and submesoscale eddy (SE) regions, respectively.

In several cases in the following analysis, horizontal (x - y) averages are calculated separately in the LO and SE regions. In these two regions, y averaging is performed only over the respective y bounds of the LO and SE regions, and averaging in the x direction is performed over the entire length of the domain since the flow fields are statistically homogeneous in the along-front direction. Horizontal spatial averages in these reduced-size regions are denoted $\langle \phi \rangle_{xy_*}$, where ϕ is a given flow or tracer quantity. Averages over the full 3-D volume, which are used to normalize some of the results for the air-sea flux tracers, are denoted $\langle \phi \rangle_{xyz}$.

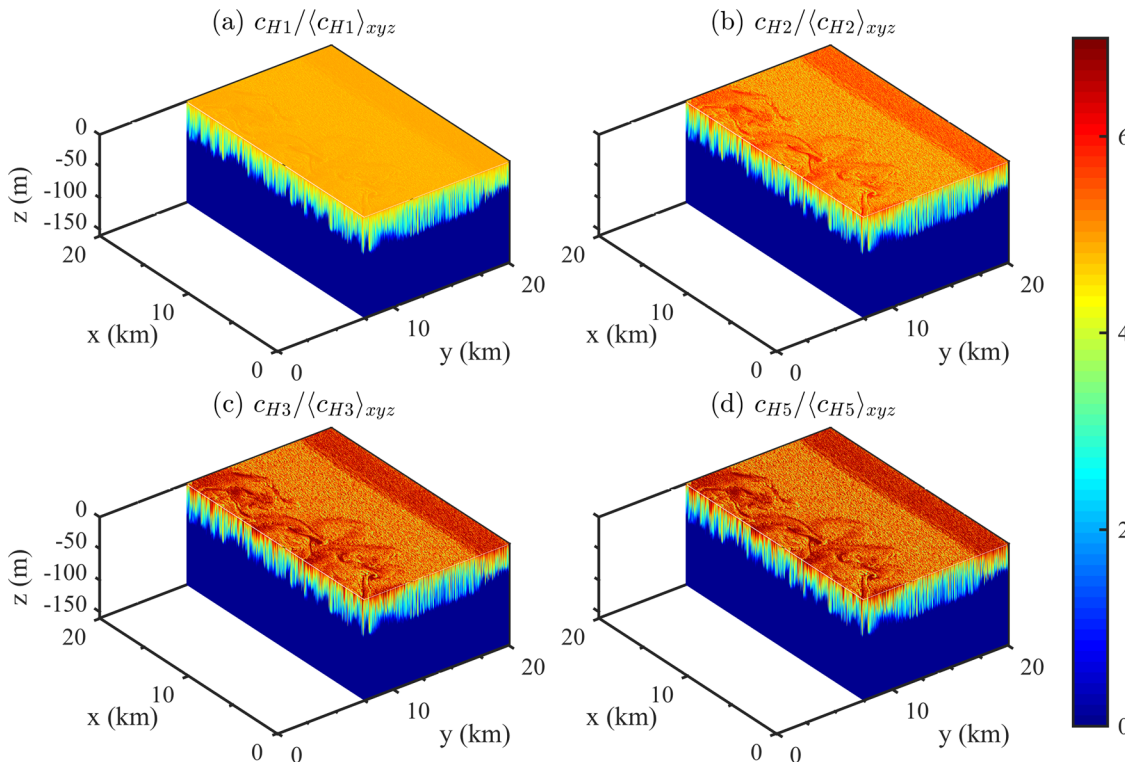


Figure 3. Instantaneous snapshots of 3-D tracer concentration fields for (a) c_{H1} , (b) c_{H2} , (c) c_{H3} , and (d) c_{H5} approximately 8 h after the tracers are introduced to the simulation. The concentrations are normalized by the volume-averaged concentration $\langle c_{Hi} \rangle_{xyz}$ for each tracer.

3.1. Air-Sea Flux Tracers

Figure 3 shows instantaneous 3-D concentration fields for c_{H1} – c_{H3} and c_{H5} approximately 8 h after the tracers are introduced to the simulation. The fields are each normalized by the average concentration calculated over the full 3-D volume. Figure 3 shows that as tracer flux rate decreases, submesoscale features are increasingly visible in the normalized concentration fields. The fastest-injected tracer, c_{H1} , rapidly saturates (defined here as reaching the concentration in air of $c_{air} = 1$) the near-surface region and then the mixed layer, resulting in overall less horizontal and vertical variability of the tracer relative to the average concentration. Tracers c_{H3} and c_{H5} (the concentration field for c_{H4} , not shown, is similar) have less uniform concentrations in the vertical direction, with higher tracer concentrations near the surface. These tracers also have considerably more horizontal submesoscale variability than the tracers with faster flux rates.

The saturation of the mixed layer for c_{H1} and c_{H2} can be seen quantitatively from the vertical profiles of average tracer concentration $\langle c_{Hi} \rangle_{xy*}$, vertical flux $\langle w' c'_{Hi} \rangle_{xy*}$, and tracer variance $\langle c'^2_{Hi} \rangle_{xy*}$ in Figure 4. Figures 4a–4c show tracer statistics after 1 h and Figures 4d–4f show statistics after 8 h. At early times, Figure 4a shows that only concentrations of c_{H1} very near the surface have begun to approach the saturated value of $c_{air} = 1$, and there is still substantial vertical mixing of c_{H1} into the lower half of the domain, as shown in Figure 4b. At later times, however, Figure 4d shows that the average concentrations of c_{H1} and c_{H2} are both close to 1 (i.e., the saturated value) down to a depth of $z \approx -40$ m, effectively spanning the entire mixed layer. As a result, the difference ($c_{air} - c_{Hi,0}$) in the surface flux rate from equation (6) is small, resulting in reduced vertical tracer transport. This can be seen explicitly by comparing Figures 4b and 4e, where at early times the vertical fluxes of c_{H1} and c_{H2} are much larger than for the other tracers, while at later times the flux of c_{H1} is actually smaller near the surface than that of both c_{H2} and c_{H3} . Similarly, comparison of Figures 4c and 4f shows that the variances of c_{H1} and c_{H2} decrease near the surface at later times and that the variance of c_{H1} is lower than the variances of c_{H2} and c_{H3} .

Saturation of the mixed layer for c_{H1} and c_{H2} at later times is also evident in the time series of total tracer concentrations shown in Figure 5. The average concentration in the mixed layer increases with time for all tracers, and an overall greater amount of tracer is present in the domain for larger k_r . Figure 5 shows,

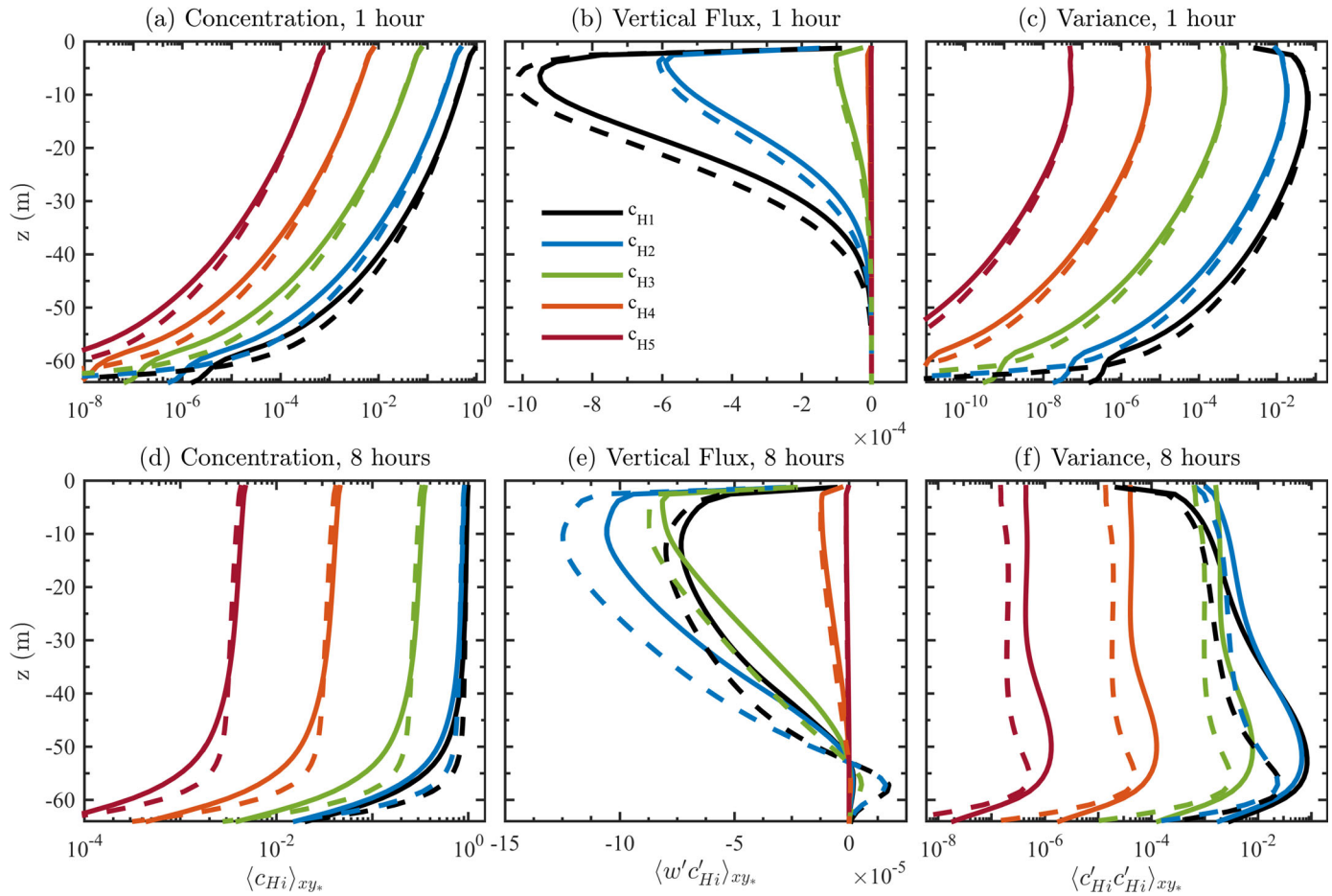


Figure 4. Vertical profiles of (a, d) average tracer concentration $\langle c_{Hi} \rangle_{xy_*}$, (b, e) vertical tracer flux $\langle w'c'_{Hi} \rangle_{xy_*}$, and (c, f) tracer variance $\langle c'^2_{Hi} \rangle_{xy_*}$, for c_{H1} – c_{H5} . Figures 4a–4c and 4d–4f show profiles 1 and 8 h after tracers are introduced to the simulation, respectively. Results are shown for the SE region (solid lines) and the LO region (dashed lines).

however, that there is a decrease in the rate at which the tracer enters the domain for c_{H1} and c_{H2} . This occurs since vertical mixing is no longer effective at reducing the near-surface tracer concentration when the mixed layer becomes saturated, resulting in smaller ($c_{air} - c_{H1,0}$) and lower surface flux rates via equation (6).

In addition to the differences between c_{H1} and c_{H5} resulting from the different surface flux rates k_i , Figures 3–5 indicate that there are also substantial differences in a given tracer field between the LO and SE regions and that these differences depend on k_i . Within the LO region in Figure 3, all tracers exhibit the same deeper penetration into the mixed layer as compared to the SE region. This is consistent with the dominance of small-scale Langmuir circulations in this region. An increase in vertical transport and a corresponding deepening of the mixed-layer depth are known characteristics of Langmuir turbulence, as is a tendency toward restratification and suppression of turbulence by submesoscale eddies [Hamlington et al., 2014]. The increased penetration depth in the LO region is shown quantitatively in Figure 4d, where average tracer concentrations remain larger to greater depths in the LO region. This increased penetration is accompanied by an increase in the vertical flux in the LO region, as shown in Figures 4b and 4e (turbulent diffusivity is also larger in the LO region than in the SE region, as will be discussed in section 4). The increased vertical flux also leads to a small decrease in surface concentrations within the LO region, as shown in Figure 4d. This represents the “flushing” of the surface layer by Langmuir turbulence, which in turn allows for an increase in the tracer flux rate into the domain at the air-sea interface, and an overall increase in tracer uptake in this region.

Figure 5 shows that the amount of tracer brought into the domain for tracer c_{H1} is larger in the LO region as compared to the SE region. This holds true for all tracers, although the difference is less pronounced for

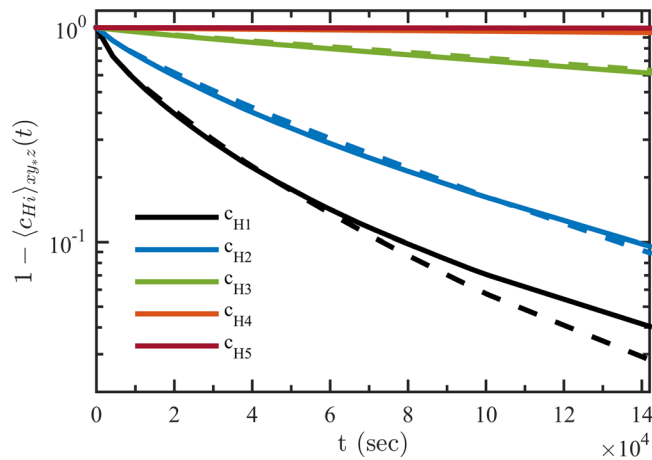


Figure 5. Time series of average tracer concentrations, $\langle c_{Hi} \rangle_{xy,z}(t)$, in the 3-D simulation volume, where averaging in the z direction is performed from $z = 0$ to -40 m. Results are shown for the SE region (solid lines) and the LO region (dashed lines).

domain. Overall, the increased vertical mixing in the LO region results in more uniform tracer concentrations, as indicated by the reduced tracer variance in the LO region as compared to the SE region shown in Figure 4f.

The dynamics are more complicated in the SE region where both large-scale eddies and small-scale Langmuir turbulence are active. Figure 3 shows that there are ridges of high tracer concentration that penetrate deep into the mixed layer, corresponding to the structures of larger submesoscale eddies and associated strong vertical jets. In between these ridges are regions near the surface dominated by smaller-scale structures similar to those in the LO region. As shown in Hamlington *et al.* [2014, Figure 13], however, there is overall less penetration of these small-scale structures to depth when compared to the LO region, resulting in a shallower mixed layer in the SE region due to restratification by submesoscale eddies. The fields of vertically integrated tracer concentration for c_{H1} – c_{H3} and c_{H5} in Figure 6 show that there are large variations in the amount of tracer that has entered the domain in the SE region, with both the largest and the smallest local amounts of tracer found in the SE region.

It is important to contrast the effects of submesoscale eddies on passive tracer uptake and transport with their effects on buoyancy transport. Submesoscale eddies consistently transport buoyancy upward and extract kinetic energy from potential energy by lifting light parcels and sinking dense parcels [Boccaletti *et al.*, 2007; Fox-Kemper *et al.*, 2008]. However, the reduction in passive tracer uptake in the SE region compared to the LO region, as shown in Figures 3–5, cannot be explained by the mechanism of potential energy extraction alone, because there is no reason why tracer concentrations should correlate with submesoscale features without an intervening mechanism. Specifically, vertical transport of passive tracers by submesoscale eddies is only *indirectly* related to vertical restratification of the mixed layer by such eddies. Figure 4e shows that vertical tracer flux is roughly 10–20% weaker in the SE region than in the LO region, but the vertical velocities associated with submesoscale eddies are only a hundredth those of Langmuir turbulence. Furthermore, in the cases where the difference is largest (e.g., c_{H1} and c_{H2}), there is little imprint of submesoscale eddies on surface concentrations (see Figure 3a), indicating that the variation in the effects of vertical transport by such eddies near the surface is overshadowed by the rate of the incoming tracer. However, submesoscale features strongly suppress turbulence through their restratifying effects. The same is true of the stable front near $y = 20$ km; this front has wind-driven restratification that suppresses turbulence (Figure 3 shows uniform surface confinement of tracer concentrations between $y = 18$ –20 km, which can be interpreted as indicative of suppressed turbulence and is discussed in more detail in Hamlington *et al.* [2014]). Care is needed in interpreting the effects of vertical fluxes created by submesoscale features, as their vertical velocity scale is large when compared to mesoscales but diminutive when compared to boundary layer turbulence. The evidence here is that their indirect, restratifying effect is significantly more important for determining vertical passive tracer fluxes than their direct passive tracer flux.

tracers with lower k_i (i.e., c_{H2} – c_{H5}). Similarly, the vertically integrated tracer concentrations in Figure 6 show that relative to tracer concentrations in the SE region, there is more tracer concentration in the LO region for c_{H1} and c_{H2} , but the difference between the LO and SE regions decreases as k_i decreases. This trend is most likely due to the requirement that vertical mixing must be fast in order to overcome fast surface flux rates for high k_i ; recall that in order for substantial vertical transport to occur via equation (6), a large difference between c_{Hi} and c_{air} must be maintained at the surface. Fast vertical circulations, which exist primarily in the LO region, are thus required to effectively introduce tracer to the

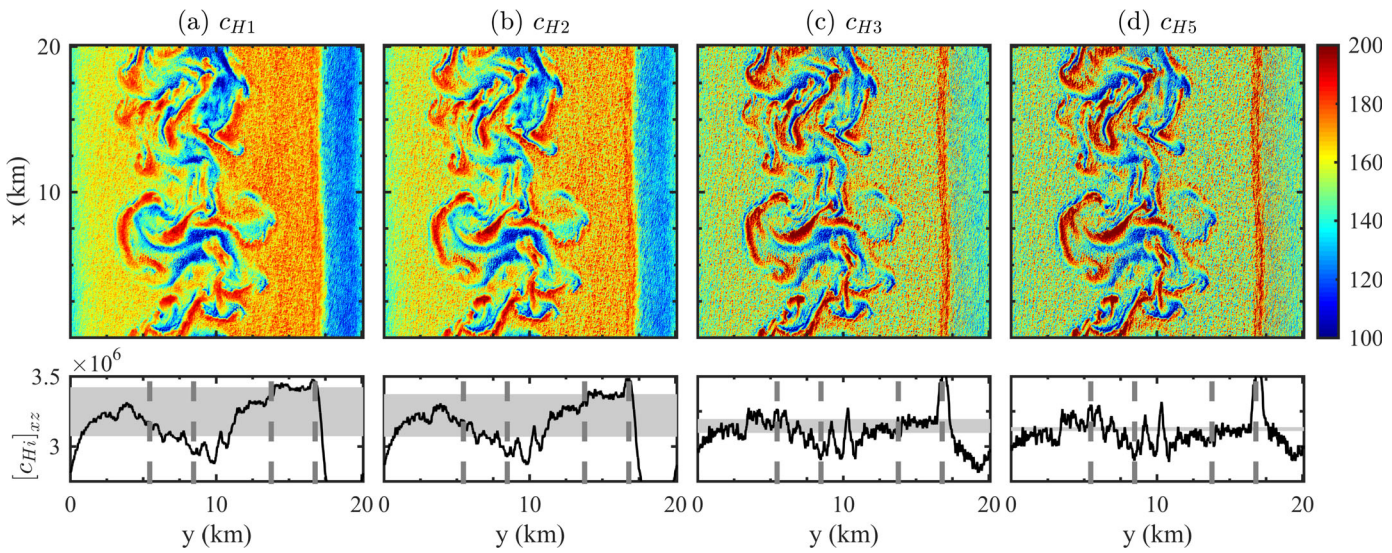


Figure 6. (top row) Vertically integrated and (bottom row) corresponding x - z -integrated tracer concentrations for (a) c_{H1} , (b) c_{H2} , (c) c_{H3} , and (d) c_{H5} approximately 8 h after the start of the simulation. The vertical integration is performed for all $N_z = 128$ grid points in the z direction and the horizontal integration is performed for all $N_x = 4096$ grid points in the x direction. The field and line plots are normalized by the full 3-D volume-averaged concentrations $\langle c_{Hi} \rangle_{xyz}$. Here $[c_{Hi}]_{xz}$ denotes a concentration integrated in both the x and z directions, vertical dashed lines indicate the SE and LO regions, and horizontal gray bands in the bottom row represent the difference between the average x - z -integrated concentrations of the LO and SE regions.

In order to further quantify the properties of air-sea flux tracers in different flow regions and for different values of k_i , tracer spectra and their scaling exponents provide quantitative measures by which distributions of tracers can be characterized. Figure 7 shows 1-D spectra in the x direction for tracers c_{H1} – c_{H3} and c_{H5} in the LO and SE regions at a depth of $z = -25$ m. The spectra are shown as a function of wave number (k), with small wave numbers corresponding to larger scales (e.g., submesoscale eddies) and larger wave numbers corresponding to smaller scales (e.g., Langmuir turbulence).

Figure 7 shows that for all k_i , there is very little large-scale energy content in the LO region, particularly when compared to the SE region. This is due to the lack of any large-scale eddies in the LO region, as can be seen from the 3-D volumes in Figure 3. In the SE region, there is more energy at large scales, with a noticeable peak in the spectra at a spatial scale of 5 km, roughly corresponding to the characteristic length scale of submesoscale eddies in the simulation. This peak is more pronounced for c_{H3} – c_{H5} where k_i is small, indicating that submesoscale eddies have a greater impact on tracer distributions when the time scales of these eddies and the surface flux rates are more closely matched (in particular, Table 2 shows that $\tau_S/\tau_i \sim 1$ for c_{H4}).

There are also much less pronounced peaks in all of the spectra in Figure 7 at a spatial scale close to 10 m, corresponding to the effects of small-scale Langmuir turbulence. In general, the spectra in the LO and SE regions are similar at small scales, but for c_{H1} where k_i is large there is overall less small-scale variance in the LO region as compared to the SE region. This is most likely due to reduced vertical transport in the SE region, which becomes particularly pronounced for high k_i , as well as to the lack of downscale transfer of tracer variance in the LO region, where significant large-scale activity is absent.

Two distinct spectral slopes exist in the large and small-scale regions of the spectra shown in Figure 7. At large scales, there is an approximate $k^{-1.3}$ slope in all of the spectra in the SE region and at small scales there is an approximate $k^{-2.5}$ scaling in both the LO and SE regions. By contrast, the scalings of buoyancy and kinetic energy spectra in the submesoscale range are k^{-2} or steeper [Hamlington et al., 2014, Figure 3], consistent with the idea that larger variance across the submesoscale range results from the extraction of potential energy by eddies. It should be noted that connecting the small-scale spectral decay with either a three-dimensional cascade or dissipative processes requires that further higher-resolution simulations be performed in the future.

3.2. Initial Source Tracers

Figure 8 shows instantaneous 3-D volumes for tracers c_{I1} and c_{I5} – c_{I7} (Table 3 shows the initialization depths). The surface tracer c_{I1} in Figure 8a is distributed throughout the vertical extent of the mixed layer on a

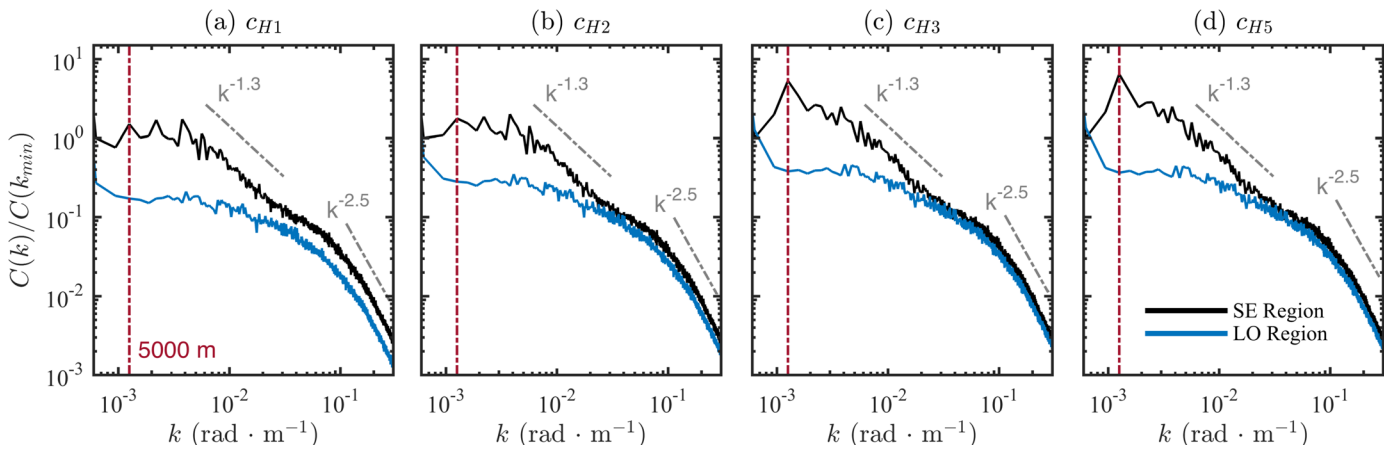


Figure 7. Spectra along the x direction at a depth of $z = -25$ m for tracers (a) c_{H1} , (b) c_{H2} , (c) c_{H3} , and (d) c_{H5} approximately 8 h after the start of the simulation. The gray dash-dotted lines show spectral slopes in the submesoscale and Langmuir-scale regions, and the vertical red dash-dotted lines show the characteristic length scale of submesoscale eddies at 5 km.

relatively short time scale, with very little indication remaining of its initial release location. This is shown quantitatively in Figure 9a where tracers c_{11} - c_{14} have essentially identical vertical profiles of average concentration $\langle c_{ij} \rangle_{xy*}$. Figure 9b shows that vertical fluxes for these four tracers are also quite similar, with $\langle w' c'_{ij} \rangle_{xy*} < 0$ over nearly the entire mixed layer. These negative fluxes represent downward transport of high tracer concentrations to greater depths throughout the mixed layer, along with entrainment of lower concentration water that is transported upward. Below the mixed-layer base, positive tracer fluxes are consistent with the gradient in tracer concentration in the partly stratified water. As a result of this vertical transport, tracers c_{11} - c_{14} are uniformly mixed down to roughly $z = -40$ m, as shown by the variance profiles in Figure 9c.

Although c_{11} - c_{14} have largely identical properties since all of these tracers exist in the upper reaches of the mixed layer where vertical mixing is generally strong, Figures 9b and 9c do show that the vertical flux and variance for c_{14} are smaller in magnitude than for c_{11} - c_{13} . These differences become even more pronounced for c_{15} - c_{17} , and Figure 8 shows that tracers c_{16} and c_{17} are still largely concentrated at their release depths, even within the LO region where mixing is enhanced. Figure 9d shows that there is reduced tracer concentration within the mixed layer as the initial source location deepens, with concentrations of c_{17} in the mixed layer nearly an order of magnitude smaller than the concentrations of c_{15} and c_{16} (the same reduced mixed-layer concentrations are also evident in Figure 8d). As a result of the lower release locations for c_{15} - c_{17} , the dominant transport of tracer concentration occurs upward, resulting in positive fluxes $\langle w' c'_{ij} \rangle_{xy*}$ for c_{16} and c_{17} in Figure 9e. As with tracers c_{11} - c_{14} , variances of c_{15} - c_{17} become relatively uniform within the mixed layer, as shown in Figure 9f.

Tracer variance is generally largest below the mixed-layer base regardless of tracer release location and concentration profile. Three phenomena explain this effect. First, there is a transition layer where the most energetic downward plumes are able to transiently, but not uniformly, inject tracer into the stratified region. Second, there are many internal waves traveling along this stratification, triggered by the initiation of the model as well as the turbulence above and the shear. Third, there are inertial oscillations and submesoscale motions capable of triggering intermittent shear instabilities. The degree to which tracer variance is increased below the mixed layer is somewhat less pronounced in the SE region than in the LO region, partly due to the greater variability in mixed-layer depth due to restratification by submesoscale eddies. Moreover, it is significant that Langmuir turbulence is able to enhance vertical mixing even for tracers released below the average location of the pycnocline (i.e., tracer c_{17}). A more thorough investigation is warranted, but is beyond the scope of this paper.

As with the air-sea flux tracers discussed in the previous section, Figures 8 and 9 also indicate that there are substantial differences in tracer properties in the LO and SE regions. Figure 8 shows that there is generally less tracer variability in the LO region as compared to the SE region and that tracers are carried to greater depths in the LO region. The deeper tracer penetration is evident from the average concentration profiles in Figure 9a. This figure also shows that tracer concentrations are generally smaller in the LO region within the mixed layer, due to the conserved nature of the c_{ij} tracers and the greater vertical extent over which the

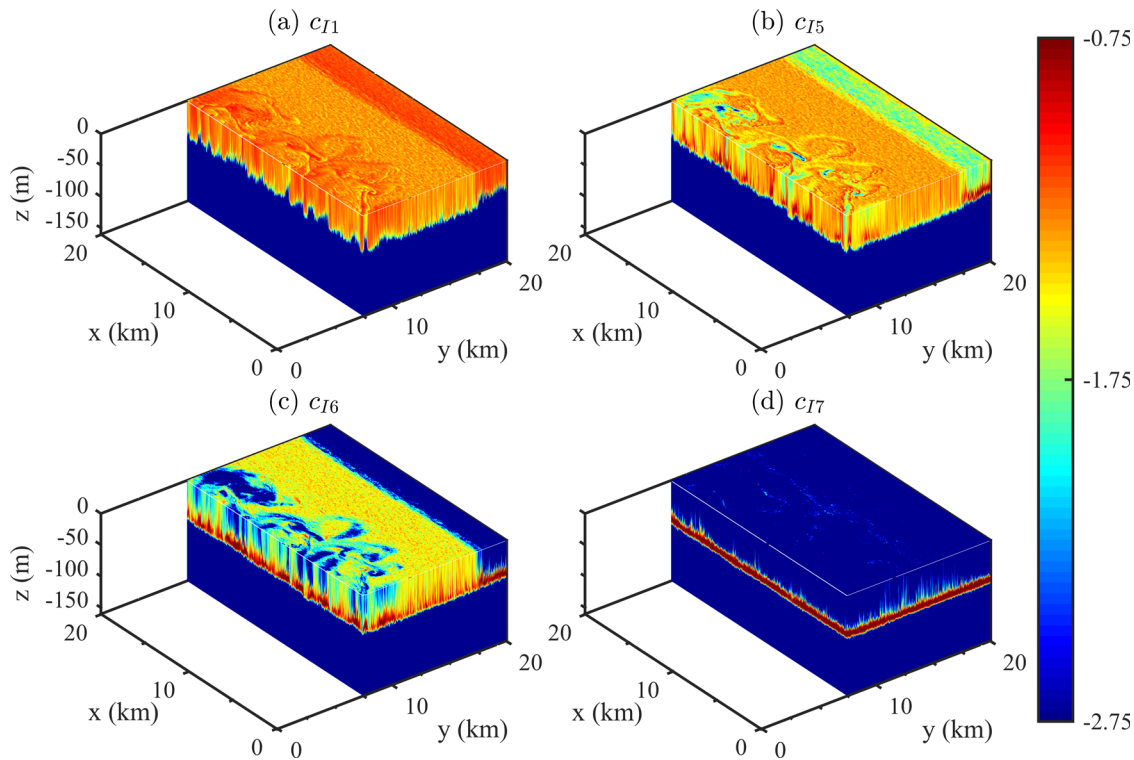


Figure 8. Instantaneous snapshots of 3-D tracer concentration fields for (a) c_{I1} , (b) c_{I5} , (c) c_{I6} , and (d) c_{I7} approximately 8 h after the tracers are introduced to the simulation. The color scale is logarithmic.

tracers are spread in the LO region. Figure 9c shows that tracer variance is smaller in the LO region, consistent with the qualitative picture provided by the 3-D volumes in Figure 8.

It is interesting to note that downward vertical flux is in fact stronger in the SE region than in the LO region, as shown in Figure 9b. This could either be due to the increased homogeneity of the tracer field in the LO region, or to the effectiveness of larger-scale vertical transport by submesoscale eddies in the SE region. However, as was argued before, the general effect of submesoscale eddies seems to be inhibition of turbulence, so the former is more likely. The other front, which is wind-restratified and stable to submesoscale features, also strongly suppresses turbulence (see Figure 8). As a result, the entrainment of tracers is significantly suppressed by both fronts, stable and unstable.

Differences between the LO and SE regions change somewhat for tracers c_{I5} - c_{I7} . Figure 8c shows that there are large regions near the unstable front where very little tracer concentration has been transported upward to the surface. By contrast to the results for c_{I1} - c_{I4} , Figure 8c actually indicates that there is more tracer above the mixed-layer base and near the surface in the LO region as compared to the SE region. This is confirmed quantitatively in Figure 9d where average tracer concentrations for c_{I6} and c_{I7} are generally larger in the LO region than in the SE region. Similarly, the vertical flux becomes substantially stronger in the LO region than in the SE region for c_{I7} , as shown in Figure 9e. These results indicate that for tracers released at depth, there is substantially enhanced vertical mixing in the LO region where Langmuir turbulence is dominant, and suppression of vertical mixing in the submesoscale region tends to outweigh the additional vertical transport by submesoscale eddies themselves. This simulation example demonstrates that the combined passive tracer vertical transport by submesoscale eddies and Langmuir turbulence is not just a simple addition of their individual fluxes; in the combined system these processes are coupled through the intermediary of their effects on stratification and shear. At least for the tracers considered here, it is therefore critical to consider the driving of turbulence by surface forcing, and turbulence-submesoscale suppression or other interactions must be resolved or well parameterized in order to capture this effect.

Another conceptual picture that emerges from Figures 8 and 9 is that of a two-layer structure within the mixed layer, based on potential vorticity and symmetric instability. *Taylor and Ferrari* [2010b] have

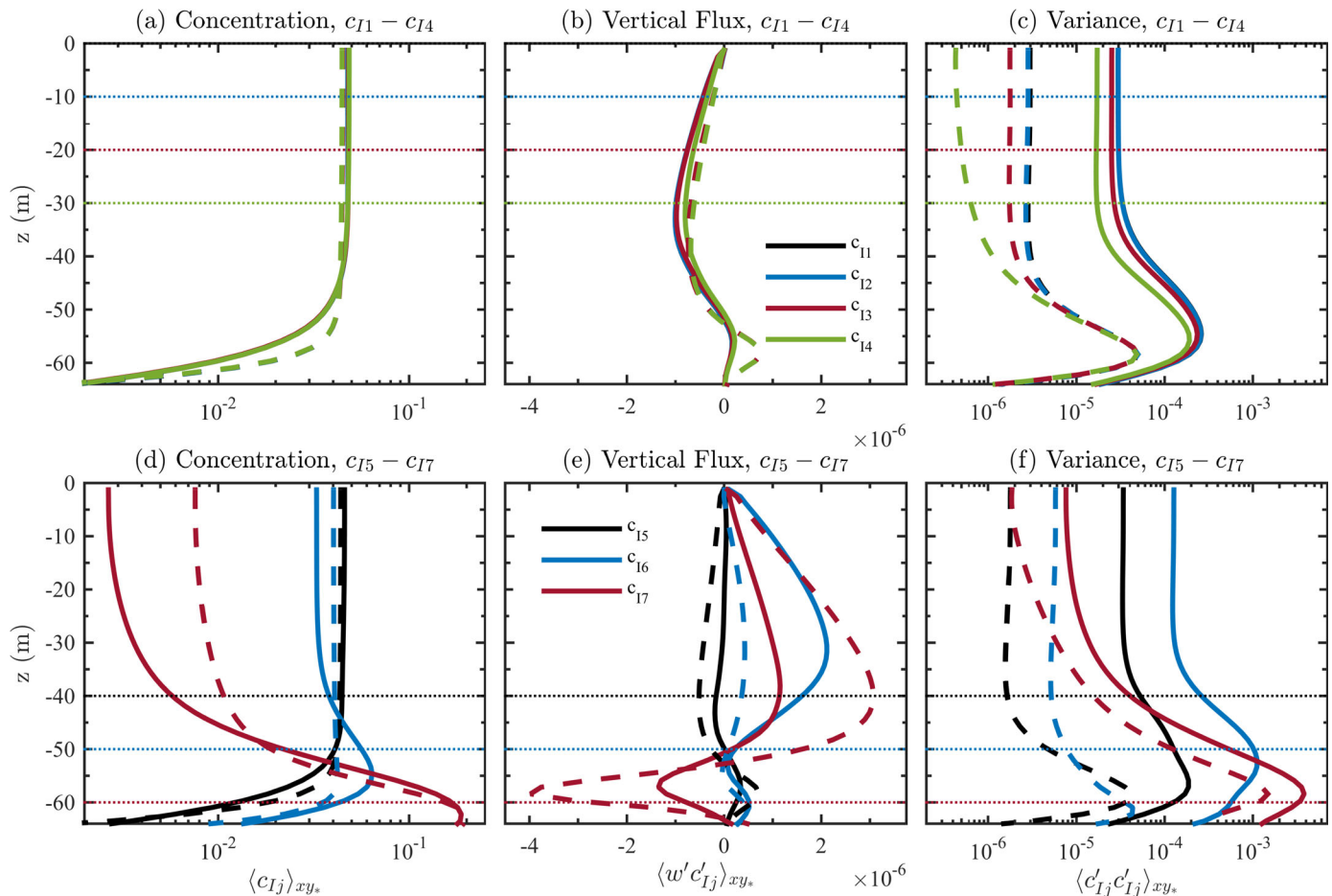


Figure 9. Vertical profiles of (a, d) average tracer concentration $\langle c_{Ij} \rangle_{xy*}$, (b, e) vertical tracer flux $\langle w' c'_{Ij} \rangle_{xy*}$, and (c, f) tracer variance $\langle c'_{Ij}^2 \rangle_{xy*}$ for c_{I1} – c_{I4} in Figures 9a–9c and for c_{I5} – c_{I7} in Figures 9d–9e. Results are shown approximately 8 h after the start of the simulation for the SE region (solid lines) and the LO region (dashed lines). Horizontal dotted lines indicate the initial locations for each tracer.

previously identified these two layers, which are distinguished by their different mechanisms of turbulence production: (i) in the *convective* layer, turbulence is generated by surface waves and fast buoyancy-driven instabilities, and is characterized by vertically uniform buoyancy fields, and (ii) in the *symmetric instability* layer, turbulence is driven by slower overturning symmetric instabilities due to slumping of lateral density gradients under the influence of rotation, and is characterized by vertical uniformity in potential vorticity. As found in Hamlington *et al.* [2014], the transition depth between these two layers, defined by the buoyancy threshold, varies substantially between the SE and LO regions. Within the LO region, the effects of the convective layer penetrate more deeply and suppress the height of the second layer such that there is little to no symmetric instability layer before the onset of interior ocean stratification. In the SE region, the convective layer is significantly shallower, allowing for larger impacts of symmetric instabilities.

The present results provide further insights into the characteristics and locations of these two layers. Tracers c_{I1} – c_{I3} have been released fully in the convective layer and thus quickly mix throughout the full vertical extent of the mixed layer. Tracers c_{I6} and c_{I7} have been released at locations that lie primarily in the symmetric instability layer, particularly in the SE region, and thus there is significantly less vertical transport than in the LO region, or than for c_{I1} – c_{I3} . Tracers c_{I4} and c_{I5} , which have initial sources at $z = -30$ and -40 m, respectively, are released near the average transition between the convective and symmetric instability layers. In combination with the results from Hamlington *et al.* [2014], the present results indicate that the localized depth at which this transition occurs varies between a maximum of roughly $z = -30$ m within the SE region and a minimum of roughly $z = -60$ m within the LO region. Within the LO region, the convective layer is deepened by the effects of Langmuir turbulence, maintaining a bridge between rapid

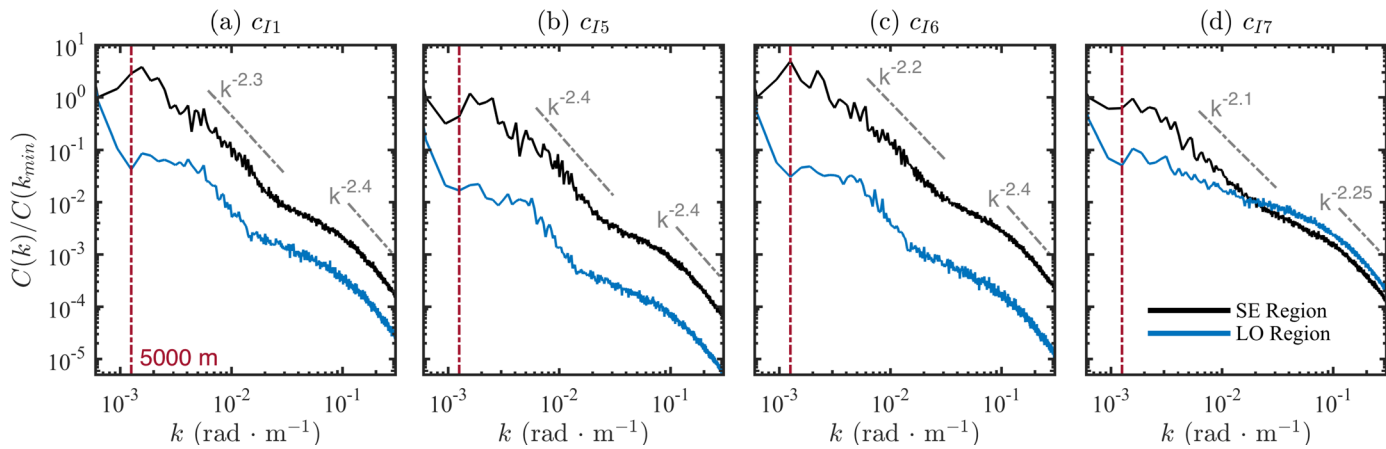


Figure 10. Spectra along the x direction at a depth of $z = -25$ m for tracers (a) c_{I1} , (b) c_{I5} , (c) c_{I6} , and (d) c_{I7} approximately 8 h after the start of the simulation. The light gray dashed lines show spectral slopes in the submesoscale and Langmuir-scale regions, and the vertical dashed lines show the characteristic length scale of submesoscale eddies at 5 km.

convective layer mixing processes and the tracer stored lower down, enabling relatively large concentrations to still be quickly pulled up to the surface. However, within the SE region, the effects of Langmuir turbulence are weaker and the convective layer is shallower, cutting off this bridge and effectively lengthening the time scale of vertical transport in this region. Even though much of the SE region allows symmetric instability, which can reach more deeply than convective instability, the overall suppression of turbulence by submesoscale restratification wins out. For tracers to be brought to the surface, they first need to be transported vertically up to the depth of the convective layer via upwelling jets and symmetric instabilities associated with submesoscale eddies, which occur in compact, localized, and intense patches on much slower time scales. From here, the convective layer can then take over and rapidly transport the tracer upward.

Finally, distributions of tracers can be quantitatively characterized using the spectra shown in Figure 10. As with the air-sea flux tracer spectra shown in Figure 7, there are spectral peaks near the submesoscale eddy characteristic length scale of 5 km and the Langmuir length scale of 10 m for the initial tracer spectra shown in Figure 10. At small scales, the spectra follow a roughly $k^{-2.4}$ scaling for all tracers, similar to the $k^{-2.5}$ scaling observed at small scales for the air-sea flux tracers in Figure 7. By contrast to the air-sea flux tracer results, however, the initial source tracers have generally steeper scaling laws in the submesoscale range (spanning $k^{-2.4}$ to $k^{-2.1}$), indicating that submesoscale feedback on air-sea fluxes plays an important role in establishing these spectra.

3.3. Multiscale Vertical Transport

As was done previously in Hamlington *et al.* [2014], two-dimensional (2-D) spectral decompositions are performed here with a wave number cutoff at $k_c = 2\pi/400$ m in order to determine the relative contributions of submesoscale and Langmuir-scale motions to vertical fluxes of buoyancy and tracers. The decompositions are calculated using 2-D horizontal fast Fourier transforms (FFTs) and 2-D circularly symmetric filtering at each depth. In addition to the usual averaging over all x , separate y subsection averaging is again performed over the SE and LO regions, allowing the relative large and small-scale contributions to vertical transport to be examined within each of these two distinctly different flow regions. Low-pass-filtered fields, which contain all wave numbers less than or equal to k_c , are assumed to be associated with 2-D submesoscale eddies. High-pass-filtered fields, which contain all wave numbers greater than k_c , are assumed to be associated with 3-D boundary layer (or Langmuir) turbulence.

Figure 11 shows depth profiles of the total, low-pass, and high-pass vertical velocity magnitude $\langle w'w' \rangle_{xy*}$, buoyancy flux $\langle w'b' \rangle_{xy*}$, and passive tracer flux $\langle w'c' \rangle_{xy*}$ for both the SE and LO regions. The scale decomposition in the LO region indicates that all vertical flux, regardless of quantity being transported, is almost entirely due to small, Langmuir-scale fluxes, with essentially no contribution coming from large scales. However, in the SE region, the scale decomposition reveals a much richer story. As was discussed in Hamlington *et al.* [2014] and as can be seen in Figure 11a, most of the total vertical velocity in the SE region is associated

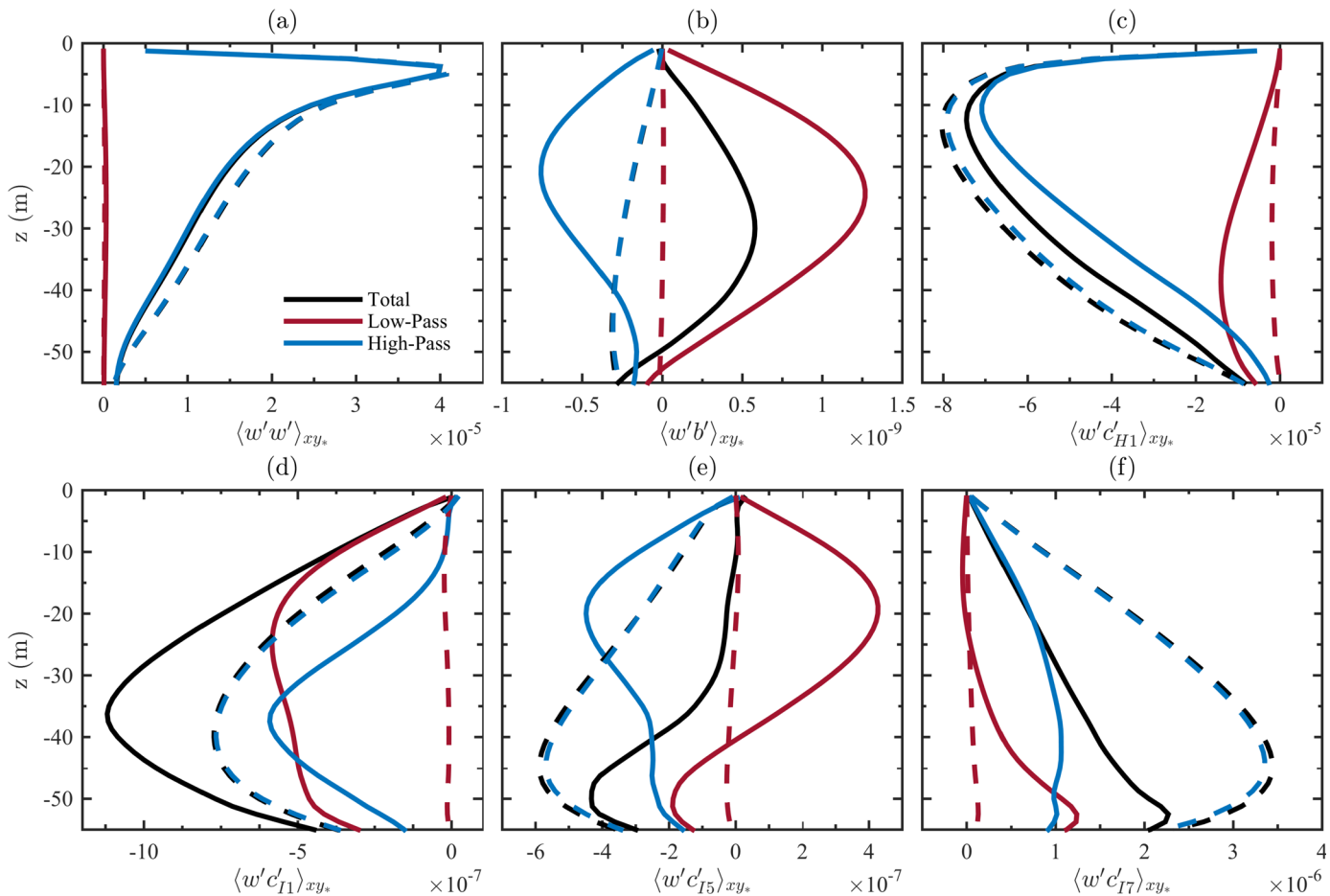


Figure 11. Multiscale vertical fluxes (a) $\langle w'w' \rangle_{xy_*}$, (b) $\langle w'b' \rangle_{xy_*}$, (c) $\langle w'c'_{H1} \rangle_{xy_*}$, (d) $\langle w'c'_{I1} \rangle_{xy_*}$, (e) $\langle w'c'_{I5} \rangle_{xy_*}$, and (f) $\langle w'c'_{I7} \rangle_{xy_*}$ approximately 8 h after the start of the simulation. Solid lines show results in the SE region and dashed lines show results in the LO region.

with small-scale motions for all depths and is primarily confined to the upper surface layers, stemming from 3-D boundary layer turbulence. Vertical flux of the active buoyancy tracer was also discussed in Hamlington *et al.* [2014], where it was found that, in contrast to the vertical velocity, the total vertical buoyancy flux exhibits substantial amplitudes all of the way down to the mixed-layer base in the SE region and remains largely positive, indicating a net restratifying effect on the mixed layer. As shown in Figure 11b and Hamlington *et al.* [2014], however, the scale decomposition reveals that the positive net transport of buoyancy is actually comprised of two opposing larger magnitude fluxes, a positive (upwelling) large-scale flux that extends deeper into the mixed layer and attempts to restratify and restore buoyancy stability by carrying warm, less dense deep waters toward the surface and a negative (downwelling) small-scale flux that attempts to homogenize the mixed layer by transporting and mixing warmer surface waters down to greater depths. Due to the active nature of the buoyancy tracer, all of this transport corresponds to changes in the potential energy of the system. Therefore, it may be sufficient, for parameterization purposes, to represent only the submesoscale restratification of buoyancy [Fox-Kemper *et al.*, 2008] and not the submesoscale transport of passive tracers [e.g., by the scalings in Bachman and Fox-Kemper, 2013]. In the present study, most effects of submesoscale eddies on passive tracers come through the suppression of turbulent mixing by increased stratification (although it may be challenging to arrive at the appropriate averaged suppression rate if submesoscale features are not resolved).

The additional coupling of passive tracers into the present analysis reveals a vastly different story than that for the active buoyancy tracer. Vertical flux of the air-sea flux tracer c_{H1} is shown in Figure 11c and other than small differences in magnitude, vertical fluxes for all air-sea flux tracers exhibit the same behavior as c_{H1} . For these tracers, the majority of the vertical flux is due to small-scale motions, which are greatest

within the surface convective layer and taper off at greater depths. The resulting transport acts to pull higher surface concentrations down to greater depths, in a consistent down-gradient direction.

The story is once again somewhat different for the passive initial source tracers. Figures 11d–11f show vertical fluxes for the surface-released tracer, c_{11} , the deep mixed layer released tracer, c_{15} , and the tracer released below the initial pycnocline, c_{17} . While each of these tracers appears to exhibit vastly different vertical profiles, a few consistent trends do appear. As with all of the other tracers in Figure 11, vertical flux in the LO region is due primarily to small-scale motions, with negligible contributions from large scales. Additionally, for all c_{ij} tracers in the SE region below the convective layer ($z \leq -40$ m), both large and small-scales fluxes are significant and similar in magnitude. By contrast, within the convective layer ($z \geq -30$ m), the similarity between the different c_{ij} tracers vanishes and a dependency on tracer release depth emerges. For the surface-released tracer in the SE region shown in Figure 11d, both large and small-scale motions work together to transport high surface concentrations to greater depths. For tracer c_{15} released deep in the mixed layer, however, Figure 11e indicates a balance between competing upwelling large-scale and downwelling small-scale motions, such that the net vertical flux for $z \geq -30$ m is close to zero. Lastly, for tracer c_{17} released below the initial pycnocline, Figure 11f shows that small-scale motions dominate large-scale motions in the mixed layer. These results all serve to show that multiscale vertical fluxes of tracers released at different depths and within different flow regions are often substantially different from each other and, contrary to suggestions in previous studies [e.g., Klein and Lapeyre, 2009] that do not take into account the effects of vertical mixing by small-scale Langmuir turbulence, cannot be explained using the same vertical flux profile as for the active buoyancy tracer.

4. Mixed-Layer Eddy Diffusivities

Results in the previous section have revealed that there are substantial differences in tracer properties and distributions depending on the type of tracer (e.g., air-sea flux or initial source), the surface flux rate, the initial source location, and the flow structure of the mixed layer (e.g., LO or SE regions). In the following, the analysis is extended to consider vertical eddy diffusivities for different tracers and different flow regions, with a view toward understanding prediction requirements for models of upper ocean tracer dynamics.

A common practice in both global and regional climate simulations is to relate tracer mixing processes at subgrid scales to known resolved-scale quantities using a subgrid-scale parameterization. The most widely used such parameterization is the gradient diffusion model, which relates turbulent vertical flux of a tracer c_i to the mean vertical gradient of the tracer's concentration as

$$\langle w' c'_i \rangle = -K_i \frac{\partial \langle c_i \rangle}{\partial z}, \quad (10)$$

where $\langle \cdot \rangle$ represents an appropriate average (defined as $\langle \cdot \rangle_{xy_*}$ in the following) and the constant of proportionality K_i is termed the vertical turbulent eddy diffusivity. Underlying equation (10) is the implicit assumption that turbulent mixing is a purely down-gradient diffusive process achieved by local, small-scale, stochastic turbulent motions. This, in turn, implies that K_i should generally be positive, and negative values of K_i typically imply a breakdown of the gradient diffusion model in equation (10). Negative diffusivities can occur in flows with active tracers, which may require a countergradient flux as opposed to the down-gradient flux represented by equation (10) [Radko, 2013], as well as in flows where submesoscale eddies restratify the mixed layer, since such eddies induce both advective and diffusive eddy transport, which are anisotropic and tracer-distribution-dependent [Bachman and Fox-Kemper, 2013; Bachman et al., 2015]. Effects due to symmetric instabilities are similarly complex [Haney et al., 2015]. Therefore, although a scalar vertical diffusivity as in equation (10) is an oversimplification, it can aid in understanding tracer transport and also mimics common tracer transport parameterization practice.

Eddy diffusivities are estimated here from equation (10) using the observed values of $\langle w' c'_i \rangle_{xy_*}$ and $\langle c_i \rangle_{xy_*}$ for the air-sea flux tracers in Figure 4 and for the initial source tracers in Figure 9. The resulting eddy diffusivities K_{Hi} for the air-sea flux tracers are shown in Figure 12 for both the LO and SE regions approximately 8 h after the start of the simulation (results at other times exhibit similar trends). Eddy diffusivities are positive throughout the mixed layer for all tracers and in both the LO and SE regions, indicating that for air-sea flux tracers, the fundamental assumption of down-gradient transport underlying equation (10) is valid. For all

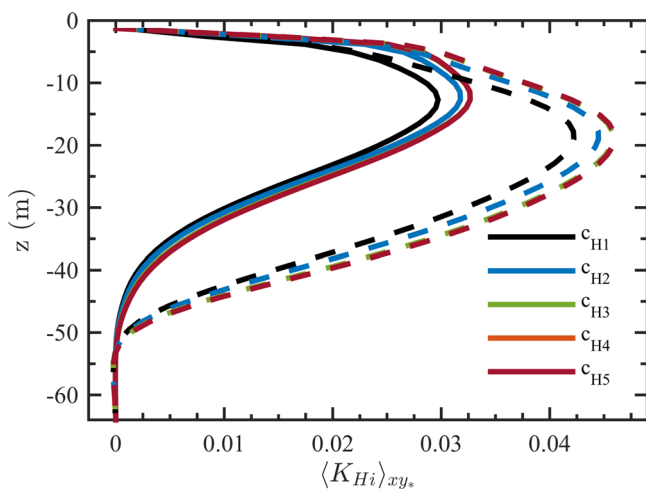


Figure 12. Profiles of vertical eddy diffusivities K_{hi} approximately 8 h after the start of the simulation for air-sea flux tracers c_{H1} – c_{H5} in the SE (solid lines) and LO (dashed lines) regions. Lines for tracers c_{H3} – c_{H5} are overlapping.

surface flux rates much lower than that of the dominant near-surface mixing rate (i.e., tracers c_{H3} – c_{H5}). However, for higher flux rates (i.e., tracers c_{H1} and c_{H2}), saturation occurs near the surface, thereby decreasing vertical transport more than the associated decrease in the vertical mean gradient (relative decreases were examined but are not shown here), resulting in slightly smaller, yet persistent, values of the vertical eddy diffusivity.

Figure 12 indicates that there are large differences in the vertical eddy diffusivity between the SE and LO regions. Figure 13 provides a more refined picture of the spatial variability of K_{hi} by showing the horizontal (x - y) field of local eddy diffusivity and the vertical (y - z) field of along-front eddy diffusivity for c_{H3} . The local eddy diffusivity is obtained by calculating $\langle w'c_i' \rangle_{xy}$ and $\langle c_i \rangle_{xy}$ over 1 km^2 horizontal regions at each value of x and y . The along-front eddy diffusivity is obtained by calculating the x -averages $\langle w'c_i' \rangle_x$ and $\langle c_i \rangle_x$ at each value of y and z . Other than small differences in magnitude and vertical extent, vertical eddy diffusivities for all of the air-sea flux tracers exhibit the same spatial structure as that shown in Figure 13 for c_{H3} .

As in Figure 12, Figure 13 shows that the eddy diffusivity field is everywhere positive at a depth of 25 m and when averaged across the x direction (this positivity also holds for all other depths in the domain), and thus agrees with the fundamental assumption underlying equation (10) that turbulent transport is down-gradient. This is to be expected given the nature of the air-sea flux tracer boundary condition, which acts as a source of tracer at the surface. Due to the surface source of air-sea flux tracers, the largest tracer concentrations occur near the surface where small-scale, diffusive-like vertical mixing is dominant and large-scale submesoscale processes that can lead to countergradient transport, such as strong upwelling plumes, are less prevalent (as previously discussed in section 3.3 and shown in Figure 11c).

Again consistent with Figure 12, Figure 13 shows that the vertical eddy diffusivity is suppressed in the SE region relative to the LO region. Moreover, Figure 13 shows that regions of suppressed convective mixed-layer depth correspond closely to regions of suppressed vertical eddy diffusivity. Mixed-layer depth is determined here [see also Hamlington et al., 2014] as the value of z where the quantity $\langle \Delta b \rangle_{xy}/(\Delta b)_c$ (for the x - y field) or $\langle \Delta b \rangle_x/(\Delta b)_c$ (for the y - z field) is approximately one, where $(\Delta b)_c = -0.53 \text{ m s}^{-2}$ and the average $\langle \cdot \rangle_{xy}$ is again over 1 km^2 horizontal subregions. Reduced vertical eddy diffusivity is thus closely associated with a shallower mixed layer in the SE region; both effects are fundamentally due to restratification of the mixed layer by submesoscale eddies. Both the stable and unstable fronts have shoaled the mixed layer, the former by Ekman buoyancy fluxes and the latter by submesoscale eddy restratification.

It is somewhat more difficult to calculate vertical eddy diffusivities for the initial source tracers c_{11} – c_{17} since the vertical gradients of $\langle c_{ij} \rangle$ are close to zero over nearly the entire mixed layer, as shown in Figures 9a and 9d. As a result, it is difficult to obtain meaningful profiles of vertical eddy diffusivities similar to Figure 12 and, consequently, only spatial maps of vertical eddy diffusivities are calculated for the initial source tracers. The resulting Figure 14 shows that vertical eddy diffusivities of the initial source tracers are vastly different

tracers, K_{hi} is largest near the surface where vertical mixing is strongest and peaks at depths of roughly $z = -13 \text{ m}$ in the SE region and $z = -20 \text{ m}$ in the LO region. Eddy diffusivities are larger in the LO region than in the SE region, consistent with the dominance of vertical transport by Langmuir turbulence in the LO region and the suppression of this turbulence in the SE region. Although there are vertical jets associated with submesoscale eddies in the SE region, the restratifying effects of these eddies suppress the mixing effects of Langmuir turbulence, resulting in an overall decrease in the amount of vertical mixing seen in this region. Figure 12 shows that eddy diffusivities are identical for tracers with

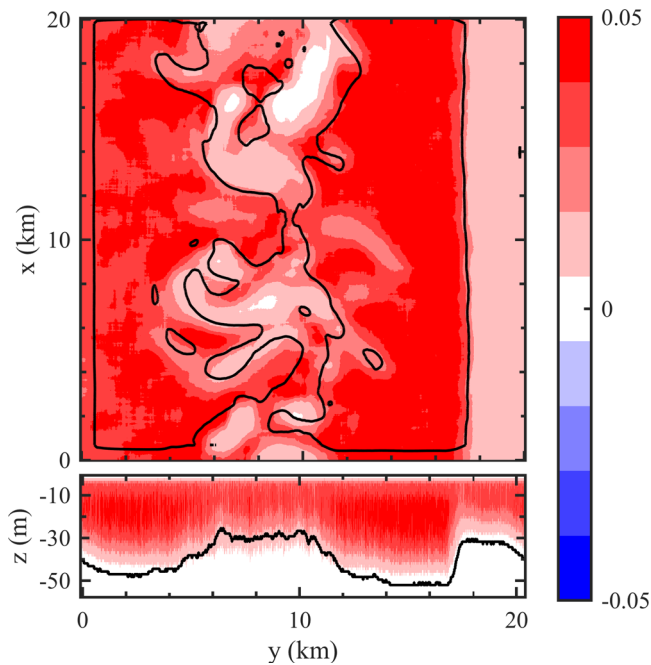


Figure 13. Fields of the vertical eddy diffusivity K_β (top) in a horizontal x - y plane at $z = -25$ m and (bottom) in a vertical y - z plane for the initial source tracer c_β approximately 8 h after the start of the simulation. The black contour lines show the depth of the mixed layer based on the buoyancy threshold $\Delta b > (\Delta b)_c$.

countergradient diffusion through nonstochastic large-scale transport by submesoscale processes, such as upwelling plumes. Hoskins [1974] proposed that in order for a flow to be unstable to symmetric instabilities, the Ertel potential vorticity, defined as

$$q = \omega_a \cdot \nabla b, \quad (11)$$

must be negative, where $\omega_a = \nabla \times \mathbf{u} + \mathbf{f}$ is the absolute vorticity. Haney *et al.* [2015] have furthered this connection to cases that include an applied Stokes drift, as in the present study.

Figure 14d shows x - y slices and x -averaged y - z plots of potential vorticity, q . Initial qualitative inspection of the corresponding K_{ij} and q fields suggests colocation of negative vertical eddy diffusivity and negative potential vorticity. This connection is made more quantitative in Figure 15, which shows the pointwise mutual information (PMI) function [Church and Hanks, 1990; Zeff *et al.*, 2003; Boeck *et al.*, 2010; Hamlington *et al.*, 2012] for vertical eddy diffusivity and potential vorticity at a depth of $z = -25$ m for tracers c_{11} , c_{16} , and c_{17} . Here the PMI function, denoted $I(q, K_{ij})$, is defined as

$$I(q, K_{ij}) = \log_{10} \left[\frac{P(q, K_{ij})}{P(q)P(K_{ij})} \right], \quad (12)$$

where $P(q)$ and $P(K_{ij})$ are marginal probability density functions and $P(q, K_{ij})$ is a joint probability density function. Positive values of $I(q, K_{ij})$ indicate a correlation between q and K_{ij} while negative values indicate an anti-correlation. When $I(q, K_{ij})$ is zero then q and K_{ij} are independent.

Figure 15 shows that for c_{11} and c_{16} , there are large positive values of $I(q, K_{ij})$ for negative eddy diffusivity and negative potential vorticity. This indicates that negative eddy diffusivity is correlated with negative potential vorticity, which means in turn that if the flow is unstable to symmetric instabilities, negative eddy diffusivities are likely to occur in the same region. It is intriguing that tracers initialized near the surface and those initialized near the mixed-layer base both exhibit this behavior. Negative potential vorticity is sometimes expected from wind-front interactions [Thomas, 2005], and these regions are frontal and oriented in roughly the down-wind direction. The potential vorticity criterion is a necessary, but not sufficient, condition for the presence of symmetric instabilities and is unchanged even in the presence of Stokes forces [Haney *et al.*, 2015]. However, turbulent transport by symmetric instabilities is significantly affected by the presence of

from one another, both in the horizontal x - y fields and the x -averaged y - z fields. These differences could be due to actual differences in eddy diffusivity or due to the different velocity fields encountered by different tracers depending on where they were released. Additionally, tracers c_{11} and c_{16} exhibit large regions of negative eddy diffusivity, particularly in the SE region, which contradicts the fundamental assumption underlying the down-gradient diffusion model in equation (10). As with the air-sea flux tracers, Figure 14 shows that a suppressed convective mixed-layer depth corresponds to a suppression of vertical eddy diffusivity, but this does not predict the location of the negative K_{ij} .

Further insights into the appearance of negative eddy diffusivities can be obtained by considering that wind-driven frontogenesis and symmetric instabilities associated with submesoscale eddies may serve as pathways for

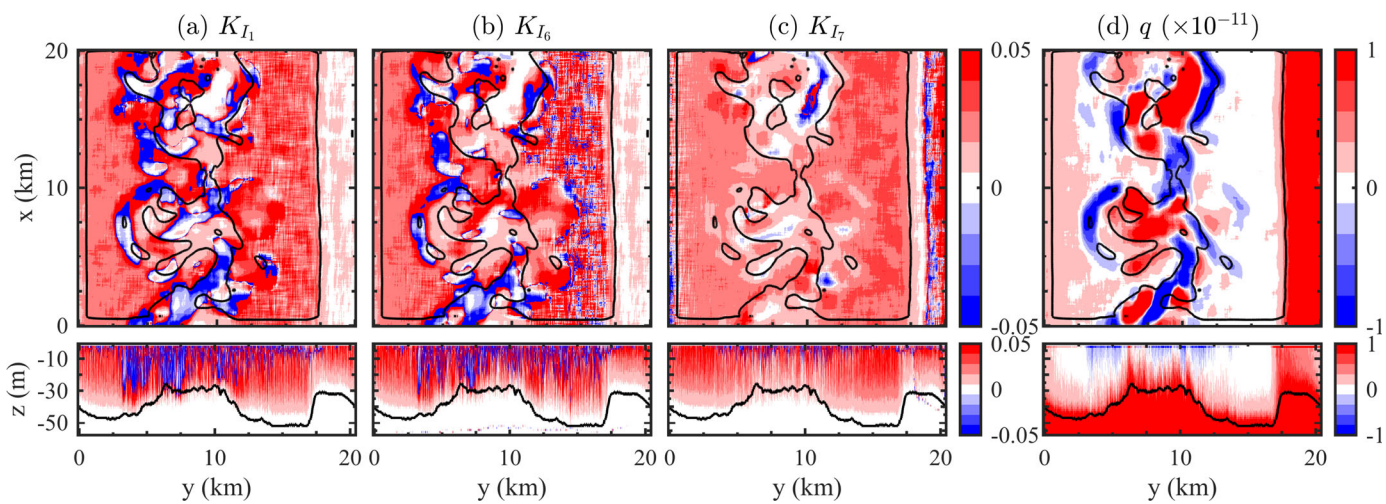


Figure 14. Same as Figure 13 but for tracers (a) c_{I1} , (b) c_{I6} , and (c) c_{I7} . Figure 14d shows the Ertel potential vorticity q defined in equation (11).

Stokes forces, and may contain considerable cross-isopycnal fluxes [Haney et al., 2015]. It should also be noted that negative potential vorticity and possibly also symmetric instabilities are not a guarantee of countergradient diffusion, as is evident from the air-sea flux tracer results where no negative eddy diffusivities are observed. It is more likely that the vertical diffusivity is a poor diagnosis of tracer transport by symmetric instability, which is typically oriented largely along isopycnals rather than vertically [Haine and Marshall, 1997], but in the presence of Stokes drift has larger cross-isopycnals directionality [Haney et al., 2015].

The correlation between negative K_j and negative q is only present during the initial phase of the tracer field evolution. Once the tracer has fully mixed throughout the mixed layer, the correlation between negative K_j and negative q fades. Closer examination of K_j at late times reveals that the vertical flux of the tracer $\langle w'c'_j \rangle$ becomes decoupled from the mean vertical gradient $\partial\langle c_j \rangle / \partial z$. The vertical gradient does, however, remain strongly correlated with q at all times. During the development phase, it can thus be hypothesized that gradients are strong and dictate the direction of tracer transport, leading to a strong correlation between negative K_j and q . As the tracers become well mixed throughout the mixed layer, both concentration gradients and fluxes become weaker and the coupling between K_j and q is lost.

5. Pseudoproduction of Phytoplankton

The initial source tracers c_{I1} and c_{I7} have been chosen in this study due to their relevance to phytoplankton production. The surface tracer c_{I1} has a release location similar to that where phytoplankton grow (i.e., near the surface due to light penetration) and tracer c_{I7} , which is initialized at $z = -60$ m, is similar to nutrients that are stored at depth and that the phytoplankton require in order to grow. It is emphasized that the idealized tracers examined in this study are not intended to be direct approximations of realistic biologically reactive tracers such as phytoplankton and nutrients. Rather, these tracers have been chosen to yield fundamental insights into fluid processes relevant to realistic tracer evolution, in the absence of potentially confounding effects due to biological reactivity.

A key characteristic of phytoplankton and nutrients is that they are both essentially passive in the water column and rely largely on physical ocean mixing processes to bring them together. In the presence of both submesoscale eddies and Langmuir turbulence, however, it is not immediately clear exactly which processes are most effective at bringing these two tracers together. Submesoscale eddies ultimately act to restratify and decrease the depth of the mixed layer, but in the process can induce compact and intense upwelling that has been shown to increase nutrient vertical transport to the surface [Strass, 1992; Spall, 1997; Haine and Marshall, 1997; Ferrari and Rudnick, 2000; Mahadevan and Archer, 2000; Levy et al., 2001; Mahadevan and Campbell, 2002, 2003; Thomas, 2005; Mahadevan and Tandon, 2006; Capet et al., 2008; Klein and Lapeyre, 2009; Mahadevan et al., 2012b]. By contrast, Langmuir turbulence deepens the convective mixed layer, helping to bridge the gap between tracers stored at depth and surface-confined tracers. Within

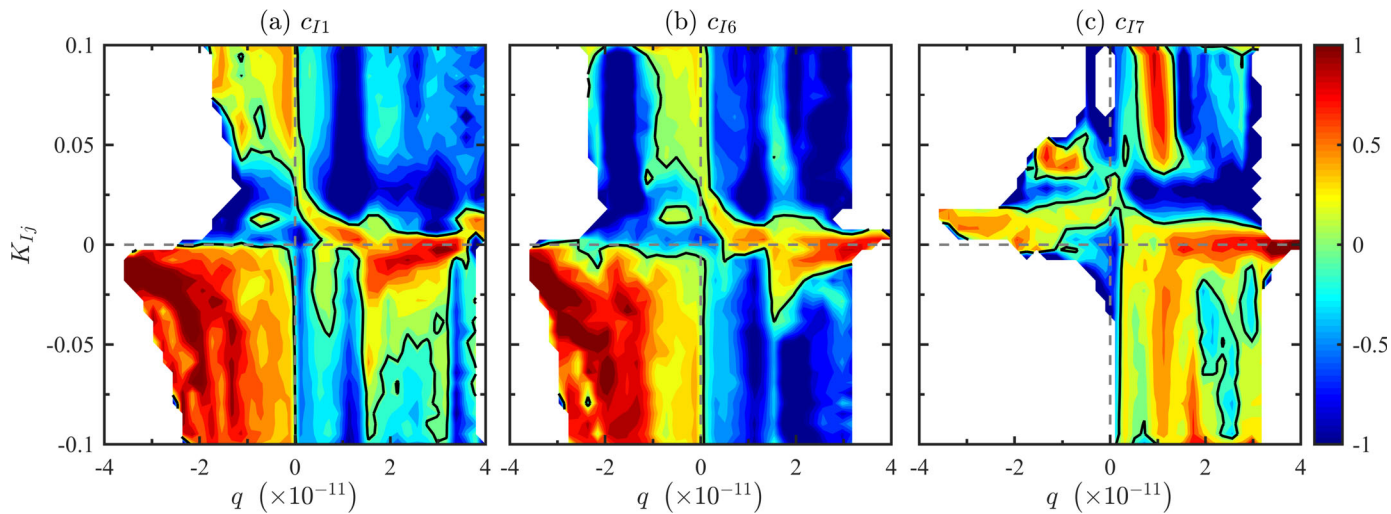


Figure 15. Pointwise mutual independence function $I(q, K_{ij})$ from equation (12) for tracers (a) c_{I1} , (b) c_{I6} , and (c) c_{I7} at a depth of $z = -25$ m approximately 8 h after the start of the simulation. Black contour lines correspond to $I(q, K_{ij}) = 0$ where K_{ij} and q are independent.

the SE region in the present study however, Langmuir suppression is the dominant effect of submesoscale activity.

Insights into how nutrients and phytoplankton are brought together in the mixed layer can be obtained by taking the product of the concentrations for c_{I1} and c_{I7} . Regions where this product is high would correspond to a higher rate of consumption of the tracer stored at depth and subsequent surface tracer growth. This product is used here as a surrogate for realistic biological production and is thus termed “pseudoproduction” in the following.

Figure 16 shows a 3-D volume of the tracer product $c_{I1} \cdot c_{I7}$ approximately 8 h after the tracers are introduced to the simulation. Upon initial examination, the overall spatial structure of the product field resembles that of the c_{I7} concentration field (see Figure 8d). This occurs since c_{I1} is nearly uniformly distributed throughout the mixed layer, and thus differences in the product are due almost completely to the distribution of the tracer stored at depth. This indicates that turbulent mixing processes that are able to pull up deeply stored tracers on relatively short time scales are most likely to promote accelerated surface tracer growth.

Notably, Figure 16 shows that there is less pseudoproduction within the SE region as compared to the LO region. The ability of Langmuir turbulence to deepen the convective mixed layer and access tracers stored at great depths promotes increased contact between a surface-released tracer and one that is stored at depth. Within the SE region, Langmuir turbulence is weakened and restratification effects are strengthened, causing the mixed-layer depth to become shallower and thus limit access of the faster convective layer to the tracer stored at depth. As a result, strong vertical upwelling plumes associated with submesoscale eddies serve as the primary mode of contact between the two tracers within this region. While these upwelling jets can contain more intense pseudoproduction, their occurrence is intermittent and their effects are sparse in comparison to the well-mixed LO region, leading to an overall smaller average pseudoproduction within the SE region. This is shown quantitatively in the vertical profiles of pseudoproduction in Figure 17, where the production within the mixed layer is larger in the LO region as compared to the SE region.

Figures 16 and 17 provide preliminary insights into processes that have the greatest potential to promote phytoplankton growth. While Langmuir turbulence in the LO region may provide greater contact between tracers at the surface and at depth, it simultaneously increases the mixed-layer depth and thus the maximum depth to which surface tracers can be transported. In the context of real-world phytoplankton production, this could result in the reduction of phytoplankton residence time above the “Sverdrup depth,” the critical depth at which photosynthesis is no longer nutrient limited, but rather light limited [Sverdrup, 1953]. In contrast, the SE region experiences a shoaling of the mixed layer, confining surface tracers to shallower

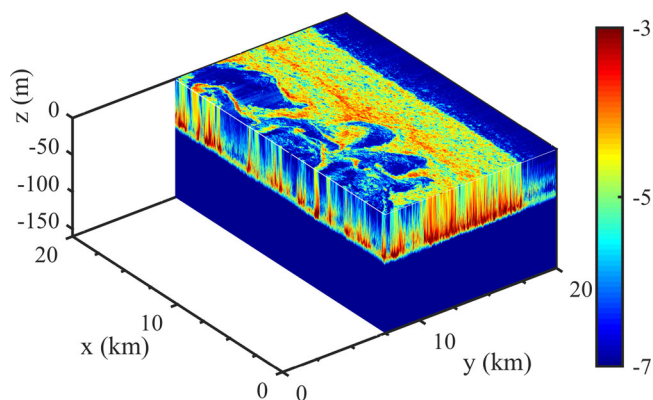


Figure 16. Instantaneous 3-D snapshot of the pseudoproduction, defined as the product $c_{I1} \cdot c_{I7}$, where tracer c_{I1} has an initial source at the surface and c_{I7} has an initial source at $z = -60$ m. Results are shown approximately 8 h after the start of the simulation and the color scale is logarithmic.

variable factors are necessary to understand the limits on growth in realistic scenarios [Sarmiento and Gruber, 2004].

6. Conclusions

In this study, a fundamental approach has been taken in order to examine the coupled effects of two different oceanic turbulent mixing processes, namely submesoscale eddies and small-scale Langmuir turbulence, on the spatial and temporal evolution of passive tracer distributions. Results indicate that the rate of air-sea tracer flux into the domain, the initial location of a tracer source, and the flow regime all have profound effects on tracer evolution.

Examination of two different flow regions, the combined submesoscale eddy and Langmuir turbulence (SE) region and the Langmuir-dominated (LO) region, reveals a substantial dependence of tracer properties on the relative strengths of restratification by submesoscale eddies and vertical mixing by Langmuir turbulence. The fast mixing enabled by small-scale Langmuir turbulence deepens the reach of the convective mixed layer, bringing more surface tracer concentration down and at-depth tracer concentration up, while the larger-scale, restratifying effects of submesoscale eddies suppress vertical mixing, except for a few strong, intermittent, and localized upwelling plumes. This dependency on flow regime is further shown to have an effect on the horizontally averaged tracer vertical eddy diffusivity.

Vertical mixing of air-sea tracers depends on the ratio of characteristic time scales associated with the tracer flux rate into the domain and near-surface mixing processes, with three different regimes evident, depending on the value of this ratio. Analysis of different air-sea tracer flux rates reveals that vertical mixing is largely independent of tracer flux rate until this ratio becomes $\mathcal{O}(1)$. At this point, the tracer saturates near-surface layers and inhibits air-sea flux of the tracer into the domain. However, entrainment of deeper water can continue to maintain surface fluxes. Outside of this characteristic time scale matching,

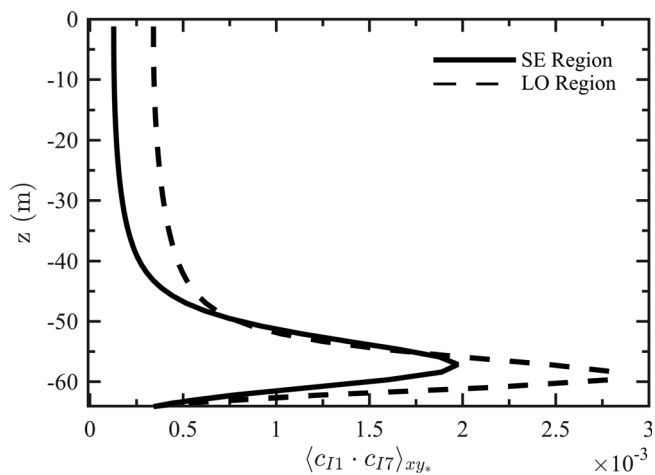


Figure 17. Vertical profiles of the x-y-averaged pseudoproduction, defined as the product $c_{I1} \times c_{I7}$, where tracer c_{I1} has an initial source at the surface and c_{I7} has an initial source at $z = -60$ m. Profiles are shown approximately 8 h after the start of the simulation for the SE region (solid line) and the LO region (dashed line).

near-surface mixing processes are sufficiently fast to flush out the surface layer, permitting an uninhibited flux of tracer into the domain. Air-sea fluxes with lower flux rates reveal significant effects of submesoscale features.

Tracers with different initial release depths exhibit vastly different distributions depending on their proximity to the mixed-layer depth. It has been found that the evolution of tracers released at depths well within the fast convective mixed layer is largely independent of the tracer initial release location. By contrast, tracers released at depths near or below the convective mixed-layer boundary exhibit vastly different spatial and temporal distributions that are heavily dependent on the initial release location as well as the shape of the bottom of the convective mixed layer.

A multiscale analysis of tracer vertical transport reveals substantial differences between vertical fluxes of different tracers, particularly in the SE region. In the LO region, essentially all of the vertical transport is performed by small-scale motions for all tracers, but in the SE region, both large and small-scale motions can play significant roles in tracer transport. This is particularly true for the initial source tracers, while the air-sea flux tracers are dominantly transported away from the surface by small-scale motions in both the SE and LO regions. Perhaps most importantly, comparisons with multiscale fluxes of buoyancy indicate that vertical fluxes of passive tracers are typically much different than vertical fluxes of buoyancy, an active tracer.

For tracers released at different initial depths, instances of negative vertical eddy diffusivity are observed, potentially corresponding to countergradient diffusion or transport by more complex structures than simply small-scale turbulent vertical mixing. Moreover, negative values of the eddy diffusivity are found to be preferentially colocated with negative potential vorticity. A mechanism resembling Stokes-influenced symmetric instability, which is indicated by the presence of negative potential vorticity [Hoskins, 1974; Haney *et al.*, 2015], may be the cause of the apparently negative eddy diffusivities, or it may be an advective aspect of frontogenesis not yet adequately understood in this context. For the initial development phase of the tracer, the correlation between negative eddy diffusivities and negative potential vorticity is strong. However, once the tracer is sufficiently mixed throughout the mixed layer, this correlation fades. During the initial development, eddy diffusivities and vertical fluxes are dictated by mean vertical gradients, with which the potential vorticity remains strongly coupled. As these gradients weaken and spread, however, eddy diffusivities and vertical fluxes are no longer strongly dictated by the gradient, leading to a decoupling with potential vorticity. These results are suggestive of countergradient diffusion occurring at certain times and locations in the present spin-down simulation, and the connection with negative potential vorticity deserves further study in the future.

Both tracer dependency on release depth and flow regime have been shown to have important consequences on productive contact between tracers that reside at the surface, such as phytoplankton, and those that are stored at depth, such as nutrients. The present results show that the tracer at depth is the limiting factor in a simple product and that the increased vertical transport occurring in the LO region promotes an overall greater average tracer product. However, determining whether this region would be more advantageous for a phytoplankton bloom relies on factoring in the averaged seasonal mixed-layer depth, average seasonal light penetration depth, as well as the reactive time scale of the phytoplankton.

Ultimately, the present study has substantial consequences for reduced-order modeling of tracer dynamics and indicates that any physically accurate passive tracer mixing parameterization should take into account dependancies related to the vertical structure of the mixed layer, the dominant flow regime (e.g., combined submesoscale-Langmuir dynamics or Langmuir-dominated dynamics), as well as the interaction between small-scale turbulent mixing and submesoscale eddies. Although many of these insights are likely to be independent of the spin-down configuration used here to generate submesoscale eddies, it is cautioned that the simulation performed in the present study represents only one particular physical configuration of the ocean (i.e., the stratification, wind strength, wave properties, etc.) over limited time period. Therefore, the findings outlined here are not necessarily universal or representative of all circumstances. Future work for different physical configurations, longer temporal durations, and more realistic ocean conditions is required in order to determine the universality of the results presented herein.

Acknowledgments

K.M.S., P.E.H., and B.F.-K. are partially supported by NSF (1258995, 1258907, and 0934737). This research was made possible in part by a grant from BP/The Gulf of Mexico Research Initiative. Contributions by Peter Sullivan to the numerical model are gratefully acknowledged. Computational data are available from the corresponding author upon request (katherine.smith-1@colorado.edu). This research utilized the Janus supercomputer, supported by NSF (award CNS-0821794) and the University of Colorado at Boulder, and the Yellowstone supercomputer (ark:/85065/d7wd3xhc) provided by NCAR's Computational and Information Systems Laboratory, sponsored by NSF.

References

- Abraham, E. R. (1998), The generation of plankton patchiness by turbulent stirring, *Nature*, 391, 577–580.
- Archer, D. (1995), Upper ocean physics as relevant to ecosystem dynamics: A tutorial, *Ecol. Appl.*, 5, 724–739.
- Bachman, S., and B. Fox-Kemper (2013), Eddy parameterization challenge suite. I: Eddy spindown, *Ocean Model.*, 64, 12–28.
- Bachman, S., B. Fox-Kemper, and F. O. Bryan (2015), A tracer-based inversion method for diagnosing eddy-induced diffusivity and advection, *Ocean Model.*, 86, 1–14, doi:10.1016/j.ocemod.2014.11.006.
- Bates, S. C., B. Fox-Kemper, S. R. Jayne, W. G. Large, S. Stevenson, and S. G. Yeager (2012), Mean biases, variability, and trends in air-sea fluxes and SST in the CCSM4, *J. Clim.*, 25(22), 7781–7801, doi:10.1175/JCLI-D-11-00442.1.
- Bees, M. A. (1998), Plankton communities and chaotic advection in dynamical models of Langmuir circulation, *Appl. Sci. Res.*, 59, 141–158.
- Benzi, R., and D. R. Nelson (2009), Fisher equation with turbulence in one dimension, *Physica D*, 238(19), 2003–2015.
- Boccaletti, G., R. Ferrari, and B. Fox-Kemper (2007), Mixed layer instabilities and restratification, *J. Phys. Oceanogr.*, 37(9), 2228–2250, doi:10.1175/JPO3101.1.
- Boeck, T., D. Krasnov, and J. Shumacher (2010), Statistics of velocity gradients in wall-bounded shear flow turbulence, *Physica D*, 239(14), 1258–1263.
- Calmet, I., and J. Magnaudet (1998), High-Schmidt number mass transfer through turbulent gas-liquid interfaces, *Int. J. Heat Fluid Flow*, 19(5), 522–532.
- Capet, X., J. C. McWilliams, M. J. Molemaker, and A. F. Shchepetkin (2008), Mesoscale to submesoscale transition in the California current system. part ii: Frontal processes, *J. Phys. Oceanogr.*, 38, 44–64.
- Church, K. W., and P. Hanks (1990), Word association norms, mutual information, and lexicography, *Comput. Linguistics*, 16(1), 22–29.
- Clayton, S. A. (2013), Physical influences on phytoplankton ecology: Models and observations, PhD thesis, Mass. Inst. of Technol., Cambridge.
- Craik, A. D. D., and S. Leibovich (1976), A rational model for Langmuir turbulence, *J. Fluid Mech.*, 73, 401–426.
- Denman, K. L. (2003), Modelling planktonic ecosystems: Parameterizing complexity, *Prog. Oceanogr.*, 57, 429–452.
- Denman, K. L., and M. R. Abbott (1994), Time scales of pattern evolution from cross-spectrum analysis of advanced very high resolution radiometer and coastal zone color scanner imagery, *J. Geophys. Res.*, 99(C4), 7433–7442.
- Donelan, M. A., J. Hamilton, and W. H. Hui (1985), Directional spectra of wind-generated waves, *Philos. Trans. R. Soc. London A*, 315(1534), 509–562.
- Ferrari, R., and D. L. Rudnick (2000), Thermohaline variability in the upper ocean, *J. Geophys. Res.*, 105(C7), 16,857–16,883.
- Follows, M. J., and R. G. Williams (2003), Physical transport of nutrients and the maintenance of biological production, in *Ocean Biogeochemistry: The Role of the Ocean Carbon Cycle in Global Change*, edited by M. Fasham, pp. 19–51, Springer, Heidelberg, Germany.
- Fox-Kemper, B., R. Ferrari, and R. Hallberg (2008), Parameterization of mixed layer eddies. Part I: Theory and diagnosis, *J. Phys. Oceanogr.*, 38(6), 1145–1165, doi:10.1175/2007JPO3792.1.
- Gjaja, I., and D. D. Holm (1996), Self-consistent Hamiltonian dynamics of wave mean-flow interaction for a rotating stratified incompressible fluid, *Physica D*, 98, 343–1887.
- Gower, J. F. R., K. L. Denman, and R. J. Holyer (1980), Phytoplankton patchiness indicates the fluctuation spectrum of mesoscale oceanic structure, *Nature*, 288, 157–159.
- Haine, T. W. N., and J. Marshall (1997), Gravitational, symmetric, and baroclinic instability of the ocean mixed layer, *J. Phys. Oceanogr.*, 28, 634–658.
- Haine, T. W. N., and J. C. Marshall (1998), Gravitational, symmetric and baroclinic instability of the ocean mixed layer, *J. Phys. Oceanogr.*, 28, 634–658.
- Hamlington, P. E., D. Krasnov, T. Boeck, and J. Schumacher (2012), Statistics of the energy dissipation rate and local enstrophy in turbulent channel flow, *Physica D*, 241, 169–177.
- Hamlington, P. E., L. P. V. Roekel, B. Fox-Kemper, K. Julien, and G. P. Chini (2014), Langmuir-submesoscale interactions: Descriptive analysis of multiscale frontal spin-down simulations, *J. Phys. Oceanogr.*, 44, 2249–2272.
- Haney, S., S. Bachman, B. Cooper, S. Kupper, K. McCaffrey, L. Van Roekel, S. Stevenson, B. Fox-Kemper, and R. Ferrari (2012), Hurricane wake restratification rates of one-, two- and three-dimensional processes, *J. Mar. Res.*, 70(6), 824–850, doi:10.1357/002224012806770937.
- Haney, S., B. Fox-Kemper, K. Julien, and A. Webb (2015), Symmetric and geostrophic instabilities in the wave-forced ocean mixed layer, *J. Phys. Oceanogr.*, 45, 3033–3056, doi:10.1175/JPO-D-15-0044.1.
- Holm, D. D. (1996), The ideal Craik-Leibovich equations, *Physica D*, 98, 415–441.
- Hoskins, B. J. (1974), The role of potential vorticity in symmetric stability and instability, *J. R. Meteorol. Soc.*, 100(425), 480–482.
- Khatiwala, S., et al. (2013), Global ocean storage of anthropogenic carbon, *Biogeosciences*, 10(4), 2169–2191.
- Klein, P., and G. Lapeyre (2009), The oceanic vertical pump induced by mesoscale and submesoscale turbulence, *Annu. Rev. Mar. Sci.*, 1, 351–375.
- Levy, M., and P. Klein (2015), Does the low frequency variability of mesoscale dynamics explain a part of the phytoplankton and zooplankton spectral variability?, *Proc. R. Soc. A*, 460, 1673–1687.
- Levy, M., P. Klein, and A. M. Treguier (2001), Impact of sub-mesoscale physics on production and subduction of phytoplankton in an oligotrophic regime, *J. Mar. Res.*, 59, 535–565.
- Lewis, D. M. (2005), A simple model of plankton population dynamics coupled with a LES of the surface mixed layer, *J. Theor. Biol.*, 234, 565–591.
- Liss, P. S., and M. T. Johnson (Eds.) (2014), *Ocean-Atmosphere Interactions of Gases and Particles*, Springer, Heidelberg, Germany.
- Mahadevan, A. (2005), Spatial heterogeneity and its relation to processes in the upper ocean, in *Ecosystem Function in Heterogeneous Landscapes*, edited by G. M. Lovett et al., pp. 165–182, Springer.
- Mahadevan, A., and D. Archer (2000), Modeling the impact of fronts and mesoscale circulation on the nutrient supply and biogeochemistry modeling the impact of fronts and mesoscale circulation on the nutrient supply and biogeochemistry of the upper ocean, *J. Geophys. Res.*, 105(C1), 1209–1225.
- Mahadevan, A., and J. W. Campbell (2002), Biogeochemical patchiness at the sea surface, *Geophys. Res. Lett.*, 29(19), 1926, doi:10.1029/2001GL014116.
- Mahadevan, A., and J. W. Campbell (2003), Biogeochemical variability at the sea surface: How it is linked to process response times, in *Handbook of Scaling Methods in Aquatic Ecology: Measurements, Analysis, Simulation*, edited by L. Seuront and P. G. Strutton, pp. 215–227, CRC Press, Boca Raton, Fla.

- Mahadevan, A., and A. Tandon (2006), An analysis of mechanisms for submesoscale vertical motion at ocean fronts, *Ocean Modell.*, 14, 241–256.
- Mahadevan, A., E. D’Asaro, C. Lee, and M. J. Perry (2012a), Eddy-driven stratification initiates North Atlantic spring phytoplankton blooms, *Science*, 337(6090), 54–58.
- Mahadevan, A., E. D’Asaro, and M. J. Perry (2012b), Eddy-driven stratification initiates North Atlantic spring phytoplankton blooms, *Science*, 337, 54–58.
- Martin, A. P., K. J. Richards, A. Bracco, and A. Provenzale (2002), Patchy productivity in the open ocean, *Global Biogeochem. Cycles*, 16(2), 1025, doi:10.1029/2001GB001449.
- McGillicuddy, D. J., Jr., A. R. Robinson, D. A. Siegel, H. W. Jannasch, R. Johnson, T. D. Dickey, J. McNeil, A. F. Michaels, and A. H. Knap (1998), Influence of mesoscale eddies on new production in the Sargasso Sea, *Nature*, 394, 263–266.
- McGillicuddy, D. J., V. K. Kosnyrev, J. P. Ryan, and J. A. Yoder (2001), Covariation of mesoscale ocean color and sea-surface temperature patterns in the Sargasso Sea, *Deep Sea Res., Part II*, 48, 1823–1836.
- McWilliams, J. C. (1985), A uniformly valid model spanning the regimes of geostrophic and isotropic, stratified turbulence: Balanced turbulence, *J. Atmos. Sci.*, 42, 1773–1774.
- McWilliams, J. C., and B. Fox-Kemper (2013), Oceanic wave-balanced surface fronts and filaments, *J. Fluid Mech.*, 730, 464–490, doi:10.1017/jfm.2013.348.
- McWilliams, J. C., P. P. Sullivan, and C. H. Moeng (1997), Langmuir turbulence in the ocean, *J. Fluid Mech.*, 334, 1–30.
- McWilliams, J. C., J. M. Restrepo, and E. Lane (2004), An asymptotic theory for the interaction of waves and currents in coastal waters, *J. Fluid Mech.*, 511, 135–178.
- McWilliams, J. C., J. Gula, M. J. Molemaker, L. Renault, and A. F. Shchepetkin (2015), Filament frontogenesis by boundary layer turbulence, *J. Phys. Oceanogr.*, 45, 1988–2005, doi:10.1175/JPO-D-14-0211.1.
- Moeng, C. H. (1984), A large-eddy-simulation model for the study of planetary boundary-layer turbulence, *J. Atmos. Sci.*, 41, 2052–2062.
- Omand, M., M. Perry, E. D’Asaro, C. Lee, N. Briggs, I. Ceticic, and A. Mahadevan (2015), Eddy-driven subduction exports particulate organic carbon from the spring bloom, *Science*, 348(6231), 222–225, doi:10.1126/science.1260062.
- Pigolotti, S., R. Benzi, M. H. Jensen, and D. R. Nelson (2012), Population genetics in compressible flows, *Phys. Rev. Lett.*, 108(12), 128102.
- Powell, T. M., and A. Okubo (1994), Turbulence, diffusion and patchiness in the sea, *Philos. Trans. R. Soc. London B*, 343, 11–18.
- Radko, T. (2013), *Double-Diffusive Convection*, Cambridge Univ. Press, Cambridge, U. K.
- Sabine, C. L., et al. (2004), The oceanic sink for anthropogenic CO₂, *Science*, 305, 367–371.
- Sarmiento, J. L., and N. Gruber (2004), *Biogeochemical Dynamics*, Princeton Univ. Press, Princeton, N. J.
- Smith, J. A. (1992), Observed growth of Langmuir circulation, *J. Geophys. Res.*, 97(C4), 5651–5664.
- Smyth, W. (1999), Dissipation-range geometry and scalar spectra in sheared stratified turbulence, *J. Fluid Mech.*, 401, 209–242.
- Spall, M. (1997), Baroclinic jets in confluent flow, *J. Phys. Oceanogr.*, 27, 381–402.
- Strass, V. (1992), Chlorophyll patchiness caused by mesoscale upwelling at fronts, *Oceanogr. Res. Pap.*, 39, 75–96.
- Strutton, P. G., N. S. Lovenduski, M. Mongin, and R. Metear (2012), Quantification of southern ocean phytoplankton biomass and primary productivity via satellite observations and biogeochemical models, *CCAMLR Sci.*, 19, 247–265.
- Sullivan, P. P., J. C. McWilliams, and C. H. Moeng (1994), A subgrid-scale model for large-eddy simulation of planetary boundary-layer flows, *Boundary Layer Meteorol.*, 71(3), 247–276.
- Sullivan, P. P., J. C. McWilliams, and W. K. Melville (2007), Surface gravity wave effects in the oceanic boundary layer, *J. Fluid Mech.*, 593, 405–452.
- Sverdrup, H. U. (1953), On conditions for the vernal blooming of phytoplankton, *J. Cons. Int. Explor. Mer.*, 18, 287–295.
- Tandon, A., and C. Garrett (1994), Mixed layer restratification due to a horizontal density gradient, *J. Phys. Oceanogr.*, 24, 1419–1424.
- Taylor, J. R., and R. Ferrari (2010a), Buoyancy and wind-driven convection at mixed layer density fronts, *J. Phys. Oceanogr.*, 40(6), 1222–1242.
- Taylor, J. R., and R. Ferrari (2010b), Buoyancy and wind-driven convection at mixed layer density fronts, *J. Phys. Oceanogr.*, 40, 1222–1242.
- Thomas, L. N. (2005), Destruction of potential vorticity by winds, *J. Phys. Oceanogr.*, 35, 2457–2466.
- Thomas, L. N., and C. M. Lee (2005), Intensification of ocean fronts by down-front winds, *J. Phys. Oceanogr.*, 35, 1086–1102.
- Thomas, L. N., A. Tandon, and A. Mahadevan (2008), Submesoscale processes and dynamics, in *Ocean Modeling in an Eddying Regime, Geophys. Monogr. Ser.*, vol. 177, edited by M. Hecht and H. Hasumi, pp. 17–38, AGU, Washington, D. C.
- Tzella, A., and P. H. Haynes (2007), Small-scale spatial structure in plankton distributions, *Biogeosciences*, 4(2), 173–179.
- Van Roekel, L. P., B. Fox-Kemper, P. P. Sullivan, P. E. Hamlington, and S. R. Haney (2012), The form and orientation of Langmuir cells for misaligned winds and waves, *J. Geophys. Res.*, 117, C05001, doi:10.1029/2011JC007516.
- Wanninkhof, R. (1992), Relationship between wind speed and gas exchange over the ocean, *J. Geophys. Res.*, 97(C5), 7373–7382.
- Watson, A. J., and J. C. Orr (2003), Carbon dioxide fluxes in the global ocean, in *Ocean Biogeochemistry: The Role of the Ocean Carbon Cycle in Global Change*, edited by M. Fasham, pp. 123–143, Springer, Heidelberg, Germany.
- Webb, A., and B. Fox-Kemper (2011), Wave spectral moments and Stokes drift estimation, *Ocean Modell.*, 40(3–4), 273–288, doi:10.1016/j.ocemod.2011.08.007.
- Webb, A., and B. Fox-Kemper (2015), Impacts of wave spreading and multidirectional waves on estimating Stokes drift, *Ocean Modell.*, 96, 49–64, doi:10.1016/j.ocemod.2014.12.007.
- Yoder, J. A., J. Aiken, R. N. Swift, F. E. Hoge, and P. M. Stegmann (1992), Spatial variability in near-surface chlorophyll a fluorescence measured by the airborne oceanographic lidar (AOL), *Deep Sea Res., Part II*, 40, 37–53.
- Zeff, B. W., D. D. Lanterman, R. McAllister, R. Roy, E. J. Kostelich, and D. P. Lathrop (2003), Measuring intense rotation and dissipation in turbulent flows, *Nature*, 421, 146–149.